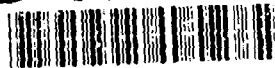


AD-A283 643



①

ARMY RESEARCH LABORATORY

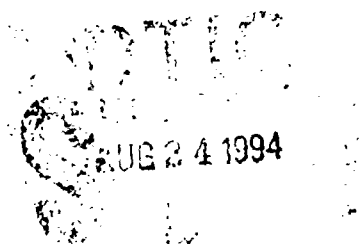


Aerodynamic Predictions for the Scorpion Parent Projectile Using a Navier-Stokes Approach

Paul Weinacht

ARL-TR-468

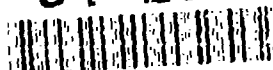
June 1994



DTIC QUALITY INSPECTED 8

APPROVED FOR PUBLIC RELEASE; DISTRIBUTION IS UNLIMITED.

94-26904



4386

94 8 23 1 1 1

NOTICES

Destroy this report when it is no longer needed. DO NOT return it to the originator.

Additional copies of this report may be obtained from the National Technical Information Service, U.S. Department of Commerce, 5285 Port Royal Road, Springfield, VA 22161.

The findings of this report are not to be construed as an official Department of the Army position, unless so designated by other authorized documents.

The use of trade names or manufacturers' names in this report does not constitute indorsement of any commercial product.

REPORT DOCUMENTATION PAGE

Form Approved
OMB No. 0704-0188

Public reporting burden for this collection of information is estimated to average 1 hour per response, including the time for reviewing instructions, searching existing data sources, gathering and maintaining the data needed, and completing and reviewing the collection of information. Send comments regarding this burden estimate or any other aspect of this collection of information, including suggestions for reducing this burden, to Washington Headquarters Service, Directorate for Information Operations and Reports, 1215 Jefferson Davis Highway, Suite 1204, Arlington, VA 22202-4302, and to the Office of Management and Budget, Paperwork Reduction Project (0704-0188), Washington, DC 20503.

1. AGENCY USE ONLY (Leave blank)		2. REPORT DATE June 1994	3. REPORT TYPE AND DATES COVERED Final, January 1990 - December 1993	
4. TITLE AND SUBTITLE Aerodynamic Predictions for the Scorpion Parent Projectile Using a Navier-Stokes Approach			5. FUNDING NUMBERS PR: 9790400.1301	
6. AUTHOR(S) Paul Weinacht				
7. PERFORMING ORGANIZATION NAME(S) AND ADDRESS(ES) U.S. Army Research Laboratory ATTN: AMSRL-WT-PB Aberdeen Proving Ground, MD 21005-5066			8. PERFORMING ORGANIZATION REPORT NUMBER	
9. SPONSORING/MONITORING AGENCY NAME(S) AND ADDRESS(ES) U.S. Army Research Laboratory ATTN: AMSRL-OP-AP-L Aberdeen Proving Ground, MD 21005-5066			10. SPONSORING/MONITORING AGENCY REPORT NUMBER ARL-TR-468	
11. SUPPLEMENTARY NOTES				
12a. DISTRIBUTION/AVAILABILITY STATEMENT Approved for public release; distribution is unlimited.			12b. DISTRIBUTION CODE	
13. ABSTRACT (Maximum 200 words) This report documents computations which were performed to determine the aerodynamic performance of several proposed designs for the Scorpion parent projectile. These aerodynamic predictions were made using a three-dimensional parabolized Navier-Stokes technique. Using the predicted aerodynamic coefficients, trajectory simulations were performed and the pitching and swerving motion of the projectile determined. This Navier-Stokes computational technique was also applied to predict the roll characteristics of one of the selected designs. Subsequently, one of the designs was fired through an aerodynamics range allowing experimental verification of the original predictions. These comparisons are also included in this report.				
14. SUBJECT TERMS Navier Stokes equations, projectiles			15. NUMBER OF PAGES 40	
			16. PRICE CODE	
17. SECURITY CLASSIFICATION OF REPORT UNCLASSIFIED	18. SECURITY CLASSIFICATION OF THIS PAGE UNCLASSIFIED	19. SECURITY CLASSIFICATION OF ABSTRACT UNCLASSIFIED	20. LIMITATION OF ABSTRACT JL	

INTENTIONALLY LEFT BLANK.

Table of Contents

	<u>Page</u>
List of Figures	v
I. INTRODUCTION	1
II. COMPUTATIONAL APPROACH	1
III. RESULTS FOR THE INITIAL DESIGNS	5
IV. PITCH-PLANE AERODYNAMICS OF IMPROVED DESIGNS	7
V. ROLL CHARACTERISTICS OF CURRENT DESIGN	8
VI. COMPARISONS BETWEEN PREDICTIONS AND FREE FLIGHT DATA	10
VII. CONCLUSION	10
References	31
List of Symbols	33

Accession For	
NTIS	<input checked="" type="checkbox"/>
DTIC	<input type="checkbox"/>
Unannounced	<input type="checkbox"/>
Justification	
By	
Date	
Approved	
Dist	
A-1	

INTENTIONALLY LEFT BLANK.

List of Figures

<u>Figure</u>		<u>Page</u>
1	Schematic of coning motion.	12
2	Schematic of projectile configuration # 1.	12
3	Schematic of projectile configuration # 2.	12
4	Variation of normal force coefficient slope with Mach number.	13
5	Variation of pitching moment coefficient slope with Mach number.	13
6	Variation of static margin with Mach number.	14
7	Variation of pitch-damping moment coefficient with Mach number.	14
8	Variation of pitch-damping force coefficient with Mach number.	15
9	Development of pitch-damping moment coefficient over projectile # 1, Mach 4.4	15
10	Pitching motion as a function of range - Projectile # 1.	16
11	Pitching motion as a function of range - Projectile # 2.	16
12	Swerving motion as a function of range - Projectile # 1.	17
13	Swerving motion as a function of range - Projectile # 2.	17
14	Schematic of flared projectile configuration.	18
15	Schematic of flared projectile with strakes.	18
16	Schematic of finned projectile configuration.	18
17	Variation of normal force coefficient slope with sweep angle.	19
18	Variation of pitching moment coefficient slope with sweep angle.	19
19	Variation of pitch-damping moment coefficient with sweep angle.	20
20	Variation of pitch-damping force coefficient with sweep angle.	20
21	Yawing-damping as a function of range for the improved designs compared with one of the initial designs.	21
22	Variation of normal force coefficient slope with Mach number, flared projectile with 25° strakes.	21
23	Variation of pitching moment coefficient slope with Mach number, flared pro- jectile with 25° strakes.	22
24	Variation of pitch-damping moment coefficient with Mach number, flared pro- jectile with 25° strakes.	22

25	Variation of pitch-damping force coefficient with Mach number, flared projectile with 25° strakes.	23
26	Pitching motion as a function of range, flared projectile with 25° strakes. . .	23
27	Swerving motion as a function of range, flared projectile with 25° strakes. .	24
28	Variation of drag coefficient with Mach number, flared projectile with 25° strakes.	24
29	Schematic showing canted strakes.	25
30	Variation of roll-producing moment coefficient with cant angle.	25
31	Variation of roll moment with spin rate for various cant angles.	26
32	Variation of roll-damping coefficient with Mach number.	26
33	Variation of equilibrium spin rate with Mach number.	27
34	Spin history for 0.5° cant angle.	27
35	Comparison of measured and predicted drag coefficient, flared projectile with 25° strakes.	28
36	Comparison of measured and predicted pitching moment coefficient, flared projectile with 25° strakes.	28
37	Comparison of measured and predicted pitch-damping moment coefficient, flared projectile with 25° strakes.	29
38	Comparison of measured and predicted normal force coefficient, flared projectile with 25° strakes.	29

I. INTRODUCTION

Segmented penetrators are being investigated because of their potential for improved terminal ballistic performance when compared to monolithic penetrators. One of the major problems associated with segmented penetrators is how to deliver the segmented penetrator to the target without significantly degrading the improved terminal ballistic performance. The Scorpion projectile was developed to investigate one possible concept for delivering segmented penetrators to a target under sponsorship by the Defense Advanced Research Projects Agency (DARPA). The concept involves a parent vehicle with segments trailing in the wake of the parent projectile. The work documented in this report is concerned with the aerodynamic design of the Scorpion parent projectile. This work was also sponsored by DARPA and was carried out in consultation with Science and Technology Associates (STA), Inc., who had overall responsibility for the projectile design. These results were previously documented in two Ballistic Research Laboratory (BRL) interim memorandum reports (BRL-IMR-939, March 1990, and BRL-IMR-957, February 1991) which were forwarded to STA, Inc. and DARPA. In 1992, the Scorpion projectile was fired through an aerodynamics range at the former BRL.* This final report formally documents the work discussed in the two previously mentioned interim reports. In addition, some experimental data obtained from the aerodynamics range firings are also included to allow benchmarking of the original predictions.

Aerodynamic predictions for preliminary design configurations, as well as for the current design, are documented. The predictions of the aerodynamics of these vehicles were performed using a sophisticated computational technique which allowed the three-dimensional viscous flow field about the body to be determined. Aerodynamic coefficients were determined from the computed flow field. These aerodynamic coefficients allow assessment of the projectile stability, pitch-damping characteristics, roll characteristics, and in-flight motion (trajectory).

In this report, the computational technique used to determine the aerodynamics of the various parent projectile designs is presented in the following section. Pitch-plane aerodynamic predictions of two initial designs are then discussed. In a subsequent section, pitch-plane aerodynamics predictions for several more recent design concepts (including the current design) are presented and compared with the predictions for the initial designs. Comparisons of the predictions with the subsequently obtained range data are also shown. Finally, predictions of the roll characteristics of the current design are presented.

II. COMPUTATIONAL APPROACH

Computation of the viscous flow field about the flared projectile configurations was accomplished by solving the thin-layer Navier-Stokes equations using the parabolized Navier-Stokes (PNS) technique of Schiff and Steger.¹ Using the parabolized Navier-Stokes technique,

*The U.S. Army Ballistic Research Laboratory was deactivated on 30 September 1992 and subsequently became a part of the U.S. Army Research Laboratory (ARL) on 1 October 1992.

computational results are obtained by marching through the grid from the projectile nose to the base. This technique is applicable in the supersonic flow regime and requires that the flow field contain no regions of flow separation in the axial direction. Because the computational approach requires only a single sweep through the computational grid, it is very efficient compared with time-marching approaches which require many sweeps through the grid.

The technique has been applied successfully to a number of projectile configurations, including axisymmetric shell,^{2,3} flared projectiles,⁴ and finned projectiles.³ Over the past several years, the computational technique has been extended to allow predictions of the roll characteristics of non-axisymmetric projectiles.^{5,6} More recent extensions to the computational approach permit predictions of the pitch-damping aerodynamic coefficients.⁷

As is standard practice, prediction of the static aerodynamic coefficients, such as pitching moment and normal force coefficients, are performed by computing the flow field about the projectile at a fixed angle of attack. The pitch-damping coefficients are determined from the side force and moment acting on the projectile undergoing steady coning motion. Steady coning motion is defined as the motion performed by a missile flying at a constant angle with respect to the free-stream velocity vector and undergoing a rotation at a constant angular velocity about a line parallel to the freestream velocity vector and coincident with the projectile center of gravity. This is shown schematically in Figure 1. Coning motion is, in fact, a specific combination of two orthogonal planar pitching motions, plus a spinning motion. From linear flight mechanics theory, it can be shown that the pitch-damping coefficients are related to the side force and moment due to steady coning motion.

The predictions of the roll characteristics are performed at 0° angle of attack. The roll-producing moment can be determined by computing the net aerodynamic roll moment acting on the projectile at zero roll rate. The roll-damping moment, which is by definition the variation of roll moment with roll rate, is determined by computing the roll moment at a number of roll rates. It is interesting to note that rolling motion as implemented here is simply coning motion at 0° angle of attack.

The flow field predictions of the projectile in steady rolling or steady coning motion have been performed in a novel rotating coordinate frame that rotates at the roll rate or coning rate of the projectile. The fluid flow relative to the rotating coordinate frame does not vary with time, allowing the steady (non-time varying) Navier-Stokes equations to be applied. To implement the rotating coordinate frame, the governing equations have been modified to include the effect of centrifugal and Coriolis forces. The steady, thin-layer Navier-Stokes equations are shown below.

$$\frac{\partial \hat{E}}{\partial \xi} + \frac{\partial \hat{F}}{\partial \eta} + \frac{\partial \hat{G}}{\partial \zeta} + \hat{H} = \frac{1}{Re} \frac{\partial \hat{S}}{\partial \zeta} \quad (1)$$

Here, \hat{E} , \hat{F} , and \hat{G} are the inviscid flux vectors, \hat{S} is the viscous flux vector, and \hat{H} is the source term containing the Coriolis and centrifugal force terms which result from the rotating coordinate frame. Each of these matrices are functions of the dependent variables represented by the vector $q(\rho, \rho u, \rho v, \rho w, e)$, where ρ and e are the density and the total energy per unit volume, and u , v , and w , are the velocity components in x , y , and z directions. The flux

terms are:

$$\hat{E} = \frac{1}{J} \begin{bmatrix} \rho U \\ \rho u U + \xi_x p \\ \rho v U \\ (\epsilon + p) U \end{bmatrix} \quad \hat{F} = \frac{1}{J} \begin{bmatrix} \rho V \\ \rho u V + \eta_x p \\ \rho v V + \eta_y p \\ \rho w V + \eta_z p \\ (\epsilon + p) V \end{bmatrix} \quad \hat{G} = \frac{1}{J} \begin{bmatrix} \rho W \\ \rho u W + \zeta_x p \\ \rho v W + \zeta_y p \\ \rho w W + \zeta_z p \\ (\epsilon + p) W \end{bmatrix} \quad (2)$$

$$\hat{H} = \frac{1}{J} \begin{bmatrix} 0 \\ H_2 \\ H_3 \\ H_4 \\ H_5 \end{bmatrix} \quad \hat{S} = \frac{1}{J} \begin{bmatrix} 0 \\ m_1 \frac{\partial u}{\partial \zeta} + m_2 \zeta_x \\ m_1 \frac{\partial v}{\partial \zeta} + m_2 \zeta_y \\ m_1 \frac{\partial w}{\partial \zeta} + m_2 \zeta_z \\ m_3 \end{bmatrix} \quad (3)$$

where

$$\begin{aligned} H_2 &= -2\Omega_c \sin \alpha \rho v - \rho \Omega_c^2 \sin^2 \alpha (x - x_{cg}) + \rho \Omega_c^2 z \sin \alpha \cos \alpha \\ H_3 &= 2\Omega_c \sin \alpha \rho u - 2\Omega_c \cos \alpha \rho w - \rho \Omega_c^2 y \sin^2 \alpha - \rho \Omega_c^2 y \cos^2 \alpha \\ H_4 &= 2\Omega_c \cos \alpha \rho v + \rho \Omega_c^2 \sin \alpha \cos \alpha (x - x_{cg}) - \rho \Omega_c^2 z \cos^2 \alpha \\ H_5 &= (-\Omega_c^2 \sin^2 \alpha (x - x_{cg}) + \Omega_c^2 z \sin \alpha \cos \alpha) \rho u - (\Omega_c^2 y \sin^2 \alpha + \Omega_c^2 y \cos^2 \alpha) \rho v \\ &\quad + (\Omega_c^2 \sin \alpha \cos \alpha (x - x_{cg}) - \Omega_c^2 z \cos^2 \alpha) \rho w \end{aligned} \quad (4)$$

$$\begin{aligned} U &= u \xi_x \\ V &= u \eta_x + v \eta_y + w \eta_z \\ W &= u \zeta_x + v \zeta_y + w \zeta_z \end{aligned} \quad (5)$$

$$\begin{aligned} m_1 &= (\mu + \mu_t)(\zeta_x^2 + \zeta_y^2 + \zeta_z^2) \\ m_2 &= \frac{1}{3}(\mu + \mu_t)(\zeta_x \frac{\partial u}{\partial \zeta} + \zeta_y \frac{\partial v}{\partial \zeta} + \zeta_z \frac{\partial w}{\partial \zeta}) \\ m_3 &= \frac{1}{(\gamma - 1)} \left(\frac{\mu}{Pr} + \frac{\mu_t}{Pr_t} \right) (\zeta_x^2 + \zeta_y^2 + \zeta_z^2) \frac{\partial a^2}{\partial \zeta} + \frac{1}{2} m_1 \frac{\partial q^2}{\partial \zeta} \\ &\quad + m_2 (u \zeta_x + v \zeta_y + w \zeta_z) \end{aligned} \quad (6)$$

$$a^2 = \frac{\gamma P}{\rho} \quad (7)$$

$$q^2 = u^2 + v^2 + w^2 \quad (8)$$

$$\begin{aligned} \xi_x &= \frac{1}{x_\xi} \\ \eta_x &= J(z_\xi y_\zeta - y_\xi z_\zeta) & \eta_y &= J(x_\xi z_\zeta) & \eta_z &= J(-x_\xi y_\zeta) \\ \zeta_x &= J(y_\xi z_\eta - z_\xi y_\eta) & \zeta_y &= J(-x_\xi z_\eta) & \zeta_z &= J(x_\xi y_\eta) \\ J &= 1 / (x_\xi (y_\eta z_\zeta - y_\zeta z_\eta)) \end{aligned} \quad (9)$$

The pressure, p , can be related to the dependent variables by applying the ideal gas law.

$$p = (\gamma - 1) \left[\epsilon - \frac{\rho}{2} q^2 \right] \quad (10)$$

The turbulent viscosity, μ_t , which appears in the viscous matrices, was computed using the Baldwin-Lomax turbulence model.⁸

The thin-layer equations are solved using the parabolized Navier-Stokes technique of Schiff and Steger.¹ Following the approach of Schiff and Steger, the governing equations, which have been modified here to include the Coriolis and centrifugal force terms, are solved using a conservative, approximately factored, implicit finite-difference numerical algorithm as formulated by Beam and Warming.⁹

Following the approach of Schiff and Steger, the equations are first linearized and placed in delta form where the equations are solved for the difference in the dependent variables rather than the variable itself. This set of equations is then factorized using the approach of Beam and Warming. The following set of equations is obtained.

$$\left[\hat{A}_s^j + (1 - \alpha) \Delta \xi (\delta_n \hat{B}^j + \hat{D}^j) \right] \Delta \hat{q}^* = RHS \quad (11)$$

$$\left[\hat{A}^j + (1 - \alpha) \Delta \xi \left(\delta_c \hat{C}^j - \frac{1}{Re} (\delta_c \hat{M}^j) \right) \right] \Delta \hat{q}^j = \hat{A}_s^j \Delta \hat{q}^* \quad (12)$$

$$\begin{aligned} RHS = & -(\hat{A}_s^j - \hat{A}_s^{j-1}) \hat{q}^j + \alpha (\hat{E}_s^j - \hat{E}_s^{j-1}) - [(\xi_x/J)^{j+1} E_p^j - (\xi_x/J)^j E_s^{j-1}] \\ & -(1 - \alpha) \Delta \xi \{ \eta_z^{j+1} (E/J)^j + \eta_v^{j+1} (F/J)^j + \eta_z^{j+1} (G/J)^j \} \\ & + \delta_c [\zeta_x^{j+1} (E/J)^j + \zeta_v^{j+1} (F/J)^j + \zeta_z^{j+1} (G/J)^j] \\ & + \hat{H}^j - \frac{1}{Re} \delta_c \hat{S}^j \} \end{aligned} \quad (13)$$

The form of the equations, as well as the notation, is similar to that used by Schiff and Steger. Here, \hat{A} , \hat{B} , \hat{C} , and \hat{M} are the Jacobian matrices of the flux vectors \hat{E} , \hat{F} , \hat{G} , and \hat{S} . Further details on the definitions of these matrices can be found in Reference 1. The important difference here is the addition of the matrices \hat{D} and \hat{H} due to the rotating coordinate system. Although the Jacobian matrix, \hat{D} , can be included in either the circumferential inversion or in the normal inversion, including this term in the circumferential inversion simplifies slightly the implementation of the shock-fitting boundary conditions.

The computations presented here were performed using a shock-fitting procedure reported by Rai and Chaussee.¹⁰ This procedure solves the five Rankine-Hugoniot jump conditions, two geometric shock-propagation conditions, and one compatibility equation to determine the values of the five dependent variables immediately behind the shock, as well as the position of the shock. By including the implicit part of the source term due to the rotating coordinate frame in the circumferential inversion, the shock-fitting procedure of Rai and Chaussee can be used without modification, as long as the correct free-stream conditions are specified as shown below in nondimensional form.

$$\begin{aligned} \rho &= 1 \\ \rho u &= M_\infty \cos \alpha + y \Omega_c \sin \alpha \\ \rho v &= \Omega_c (z \cos \alpha - (x - x_{cg}) \sin \alpha) \\ \rho w &= M_\infty \sin \alpha - y \Omega_c \cos \alpha \end{aligned}$$

$$e = p_{\infty}/(\gamma - 1) + \frac{1}{2}\{(M_{\infty}\cos\alpha + y\Omega_c\sin\alpha)^2 + (\Omega_c(z\cos\alpha - (x - x_{cg})\sin\alpha))^2 + (M_{\infty}\sin\alpha - y\Omega_c\cos\alpha)^2\} \quad (14)$$

The computational results presented here were obtained using a grid that consisted of 60 points between the body and the shock. In the circumferential direction, gridding was performed over the entire body (360°). For the axisymmetric bodies 72 circumferential grid points were used. On the finned or straked portions of the projectiles, 300 circumferential grid points were used. In the marching (axial) direction, 80 marching planes were required for each caliber of body length.

The computations were performed on a Cray X-MP supercomputer. For the flared projectiles, solutions for a single set of conditions (Mach number, roll rate, angle of attack, etc.) required 30 to 40 minutes of CPU time. Solutions for the finned or straked projectiles required about 90 minutes of CPU due to the increased grid resolution required.

III. RESULTS FOR THE INITIAL DESIGNS

In this section, the aerodynamic performance of the initial designs is discussed. Schematics of the first two design configurations are shown in Figures 2 and 3. Computations have been performed to determine the static and dynamic pitch-plane aerodynamic coefficients for both of the proposed flared projectile designs. Using the predicted aerodynamic coefficients, trajectory simulations have been performed and the pitching and swerving motion of the projectile has been determined. The computations were performed over a range of Mach numbers ($M_{\infty} = 3.5$ to 4.4) for free-flight (sea-level) atmospheric conditions.

Predictions of the normal force and pitching moment coefficient slopes were obtained across the Mach number range of interest for both projectiles. These predictions are shown in Figures 4 and 5. As was mentioned previously, projectile configuration # 2 has a slightly longer cylindrical body than does configuration # 1. This additional cylindrical portion of the body does not contribute to the lift of the body. Thus, the normal force coefficient slope of both projectiles is nearly identical. The pitching moment coefficient slope of projectile # 2 is slightly higher than that of projectile # 1 because of the favorable location of the center of gravity relative to the center of pressure. The predictions indicate that both configurations will be statically stable.

Figure 6 shows the variation of the static margin with Mach number for both projectiles. The static margin, defined as the distance between the center of pressure and the center of gravity, is normalized by the cylinder diameter. The predictions of static margin are in good agreement with previous predictions.¹¹

The computed variations of pitch-damping moment and force coefficients are shown in Figures 7 and 8. The predicted pitch-damping force and moment coefficients are determined from the side force and moment acting on the projectile undergoing steady coning motion. This allows a steady flow computation to be used to predict an aerodynamic coefficient which is usually associated with unsteady or time-dependent motion. Projectile # 2 has a higher

pitch-damping moment coefficient because of its larger length-to-diameter ratio. Despite the larger pitch-damping moment coefficient, both projectiles have similar damping rates. This occurs because the larger pitch-damping of projectile # 2 is offset by its increased moment of inertia. The pitch-damping force coefficient, as shown in Figure 8, does not have a significant effect on the motion of the projectile. However, this coefficient is required to determine the variation of the pitch-damping moment coefficient with changes in center of gravity location. These relations have been determined by Murphy.¹²

Figure 9 shows the development of the pitch-damping moment coefficient over projectile configuration # 1 at Mach 4.4. The figure shows that most of the pitch-damping moment is produced by the flared portion of the body.

Using the aerodynamic coefficient predictions, the motion of the projectile undergoing planar pitching motion was determined for both projectiles and is shown in Figures 10 and 11. The amplitude of the pitching motion has been scaled by the initial yaw level, α_0 . The initial yaw level, as well as the phase angle of the yawing motion, is not known. These parameters are functions of the gun system, individual gun tube, sabot package, and other factors. Because of this, these plots should not be used to determine the range position at which zero yaw level occurs. Experience has shown that initial yaw levels as high as 3° might be expected.¹³

Both Figures 10 and 11 show that the pitching motion damps to about 40% of the initial yaw level at about 200 m from the gun. The damping of both projectiles is similar, even though projectile # 2 has a pitch-damping moment coefficient that is 20% greater than projectile # 1. This is because the damping rate, λ , is also a function of the mass, m , and moment of inertia, I , of the body, as shown in equation 15. The increased pitch-damping moment coefficient of projectile # 2 is offset by its increased moment of inertia. The net effect is a difference in damping rate of less than 4%.

$$\lambda = \frac{\rho S_{ref} D}{2m} [C_{La} - C_D - \frac{m D^2}{I} (C_{mq} + C_{m\dot{\alpha}})] \quad (15)$$

The pitching rate of the projectiles is similar, though at 300 m the projectiles are out of phase by half a cycle.

The fluctuating part of the swerving motion due to planar pitching motion is shown in Figures 12 and 13. These figures show the motion of the projectile center of gravity about the mean flight path of the projectile. The displacement of the projectile center of gravity about the flight path due to this motion is less than a tenth of a caliber for 1° of initial yaw. Of course, the amount of displacement is proportional to the initial yaw level.

The motion of the center of the projectile base is also shown on these figures. The motion of the base can be decomposed into two components; the motion of the center of gravity, and the motion of the base relative to the center of gravity. In planar pitching motion, the center of gravity responds half a cycle out of phase to the pitching motion. The pitching motion also produces a deflection of the base relative to the center of gravity. This motion is in the same direction as the center of gravity displacement. The sum of these motions produces deflections of about 0.15 calibers per degree of initial yaw at a position 200 m from the gun.

The swerving motion of the projectile center of gravity and the motion of the base center is similar for both projectiles.

IV. PITCH-PLANE AERODYNAMICS OF IMPROVED DESIGNS

Following the analysis of the aerodynamic performance of the two initial designs, three additional design concepts were proposed to improve the pitch-damping performance of the projectile. Each of these three designs had a larger length-to-diameter ratio compared with the two initial configurations. Additionally, the cone angle of the nose was increased slightly over initial configurations. This was done to move the center of gravity and the center of pressure due to nose lift further forward. Both of these changes should improve the pitch-damping performance. The forebodies on each of the three design configurations were identical. The tail sections of the three designs consisted respectively of a 15° flare, a 15° flare with six strakes, and a fin hub with six fins. The strake and fin sweep angles (angle between the projectile axis and fin leading edge) was initially specified as 30° . However, in this study, the sweep angle was allowed to vary between 15° and 30° so that the effect of fin sweep could be considered. The three designs are shown schematically in Figures 14-16. Aerodynamic predictions for these design configurations were performed at Mach 4.4 for free-flight atmospheric conditions.

The predictions of the normal force and pitching moment coefficient slopes and the pitch-damping force and moment coefficients for the three designs are shown in Figures 17-20. These results are displayed as a function of fin sweep or strake sweep angle. The effect of changes in center of gravity due to variations in the fin or strake sweep angle have not been considered in the aerodynamic predictions. These changes are probably small, given that the center of gravity location of the flared projectile and the flared projectile with 30° strakes are similar.

The aerodynamic coefficients for the flared projectile with strakes increase as the sweep angle of the strakes increases. The increases in these coefficients is greatest between 17.5° and 25° sweep angles. There is little change in the aerodynamics coefficients between 25° and 30° sweep angle. The aerodynamic coefficients for the flared projectile with strakes approaches the values for the flared projectile as the sweep angle is decreased. This is expected since the flared projectile with strakes reduces to a flared projectile when the strake angle is equal to the flare angle (15°).

The finned projectile shows a small variation in the aerodynamic coefficients with increasing sweep angle. The normal force and pitching moment slopes for the finned projectile are slightly greater than those for the flared projectile. The pitch-damping coefficients, however, are significantly less than those for either the flared projectile or the flared projectile with strakes.

The predicted pitch-damping coefficients have been used to determine the yaw-damping as a function of range for each of the three designs (Figure 21). The yaw-damping predictions are compared with the predictions for initial design projectile # 1. The flared projectile with

strakes has the best yaw-damping performance. The yaw level at 200 m from the gun is half that of the initial design. The flared projectile shows some improvement in yaw-damping over the initial design, while the finned projectile shows only a marginal improvement. It should be noted, however, that the finned projectile has considerably less drag than any of the flared projectile designs. This makes fins more suitable for tactical configurations which must maintain their velocity over longer ranges than are required for the Scorpion projectile.

In the current application, one of the primary benefits of the flare is the increase in the size of the wake region. It is believed that the increased size of the wake region may decrease the aerodynamic interaction of the trailing segments. Because the finned configuration doesn't provide any benefit in pitch-damping compared with the flared projectiles and because the finned projectiles will have a smaller and possibly more complex wake region, they are probably not suitable for the current application.

Based on these aerodynamic predictions discussed here, STA, Inc. has chosen to proceed with the flared projectile with 25° strakes. The 25° strakes yield almost identical performance to the 30° straked projectile and is less likely to encounter interference problems due to sabot discard.

The variation in the normal force, pitching moment, and pitch-damping coefficients with Mach number for the flared projectile with 25° strakes is shown in Figures 22-25. The coefficients show moderate variations between Mach 3 and Mach 5. The pitching and swerving motion of this design are shown in Figures 26 and 27. These figures show that the pitching motion and the swerving motion at the center of gravity and projectile base have been reduced compared with the initial design configurations. Due to an increase in the pitching moment coefficient, the projectile also has somewhat higher pitching rate compared with the initial designs.

Predictions of the forebody drag have been made with the parabolized Navier-Stokes (PNS) code. This code is not suitable for computing the flow in the base region of the projectile; hence, the base drag could not be determined using this approach. Estimates of the base drag were obtained using the Naval Surface Weapons Center (NSWC) aerodynamic design code.¹⁴ The base drag component was added to the PNS forebody drag predictions to obtain predictions of the total zero yaw drag of the projectile. These predictions are shown in Figure 28. The increase in drag for this configuration over the initial configurations is due primarily to the steeper flare. Increasing the flare angle from 12° to 15° added about 30% to the forebody drag. The addition of the strakes to the flare added about 5% additional forebody drag.

V. ROLL CHARACTERISTICS OF CURRENT DESIGN

Statically stable projectiles, such as the configurations examined here, are designed to fly at a small roll rate. This is done to minimize the effect of asymmetries which may occur during manufacturing. Computations were performed to determine the roll characteristics of the flared projectile with 25° swept strakes. The strakes were canted to generate a roll-producing moment. Figure 29 is a schematic showing the nature of the canted strakes. The

computations were performed over a range of supersonic Mach numbers and 0° angle of attack for free-flight atmospheric conditions.

Computations were first performed to predict the effect of cant angle on the roll-producing moment. Figure 30 shows the variation in the roll-producing moment with cant angle at Mach 4.4. The variation of the roll-producing moment shows a slightly nonlinear variation with cant angle. The largest nonlinear variations were observed at the higher Mach numbers examined here. The curve is well-fit using the nonlinear form shown below.

$$C_{l_o} = C_{l_o} \delta + C_{l_{o2}} |\delta| \delta \quad (16)$$

The coefficients C_{l_o} and $C_{l_{o2}}$ were determined using a least-squares fitting procedure. These coefficients are shown in Table 1. Attempts were made to fit the data with a cubic term instead of the quadratic term, however, the quadratic term provided a better fit.

Table 1. Roll-Producing Moment Coefficients as a Function of Mach Number

MACH NUMBER	C_{l_o}	$C_{l_{o2}}$
3.0	5.18	7.32
3.5	5.96	1.45
4.0	6.13	-1.91
4.4	5.98	24.18
5.0	6.61	27.45

The roll-damping moment, C_{l_p} , was determined by running a series of computations at various spin rates. The variation in the net roll moment with spin rate at Mach 4.4 is shown in Figure 31. Computational results are shown for three different cant angles, 0.25°, 0.5°, and 0.625°. The variation of the net roll moment with spin rate (by definition the roll-damping moment), is seen to be linear and independent of cant angle. For Mach 4.4, the predicted roll-damping moment coefficient is 8.95. The variation in the roll-damping coefficient with Mach number is shown in Figure 32.

Figure 31 also shows that the equilibrium spin rate (spin rate at which the net roll moment is zero) increases with the cant angle. The variation in the equilibrium spin rate with Mach number for the 0.5° canted strake is shown in Figure 33. Also shown here is the variation of the nondimensional pitching frequency with Mach number. The equilibrium spin rate for the 0.5° canted strakes is below the pitching frequency across the Mach number range.

Figure 34 shows the predicted roll history of the projectile for the 0.5° canted strakes, launched at Mach 4.4 and zero initial spin rate. The effect of the variation in the projectile velocity due to drag has been included in the prediction. Also shown is the yawing frequency of the projectile. The yawing frequency varies slightly with range due to the change in the projectile velocity due to drag. The spin history of the projectile is well below the pitching frequency over the first 200 m of flight.

VI. COMPARISONS BETWEEN PREDICTIONS AND FREE FLIGHT DATA

In 1992, a number of the 25° straked flare projectiles were fired through BRL's Transonic Range. The primary purpose of the tests was to examine the segmentation process as it occurred in flight. However, the projectile did fly over 100 m before the segmentation process was initiated. Standard aerodynamic range measurements were obtained throughout the flight and, from this data, it was possible to extract the aerodynamic forces and moments. To avoid disturbances from the initiation of the segmentation process, only measurements from the first three groups of shadowgraph stations were used for extracting the aerodynamic data on the parent projectile. Additionally, many of the rounds had very low yaw and little useful data on the aerodynamics of the parent projectile was obtained. It should be emphasized that the test was primarily to observe the segmentation process and, to this end, the projectile was designed to fly with a minimum amount of yaw.

Most of the rounds yielded good data on the drag coefficient of the round. Comparison of the predicted and measured drag coefficients are shown in Figure 35. Both results show a similar trend with Mach number with the prediction about 5% lower than the measurement. This is a reasonable comparison given that predicted base drag was based on estimates from a fast design code.

Comparisons of pitching moment, pitch-damping moment, and normal force coefficients with the range data are made in Figures 36-38. Since the pitching moment and pitch-damping moment are dependent on the center of gravity location, the results also include predictions of these coefficients at the center of gravity location as measured before firing. The center of gravity location as tested was 0.27 calibers forward of the original design center of gravity location. The new aerodynamic predictions were obtained using the center of gravity translation relations and the original base line aerodynamic coefficients. The predictions are generally within the scatter of the range data. The accuracy of the range data for these coefficients was diminished somewhat due to the low yaw experienced by the projectile and due to the shortened trajectory over which aerodynamic data on the parent projectile could be obtained. Again, it is emphasized that extracting aerodynamic data on the parent projectile was a secondary consideration for the test.

VII. CONCLUSION

Aerodynamic coefficient predictions have been obtained for several proposed designs for the Scorpion parent projectile. These aerodynamic coefficient predictions were used to assess the stability and damping performance of the designs. The predictions show that the flared projectile with 25° strakes yielded better damping performance compared to the initial designs.

Predictions of the roll characteristics of the flared projectile with 25° strakes were also made. The results show that canting the strakes at 0.5° with respect to the projectile axis

will produce a roll rate which is below the pitching frequency of the projectile during the first 250 m of flight.

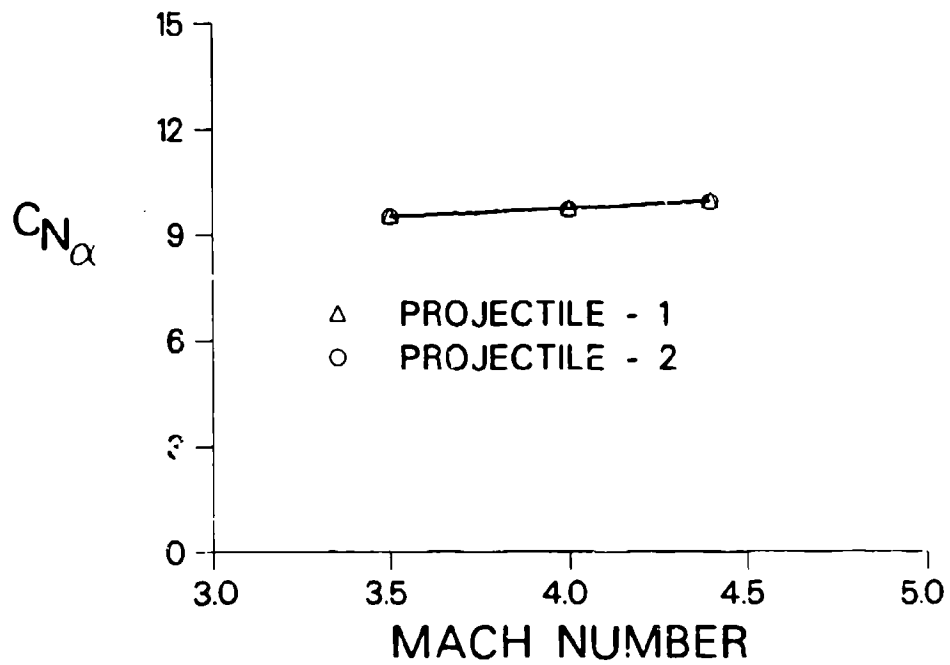


Figure 4. Variation of normal force coefficient slope with Mach number.

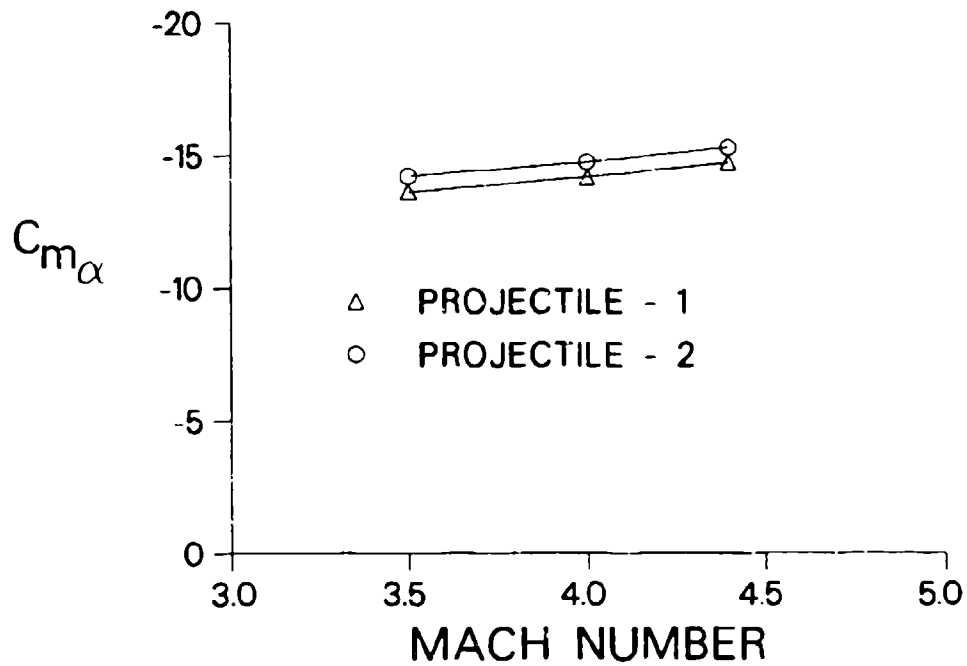


Figure 5. Variation of pitching moment coefficient slope with Mach number.

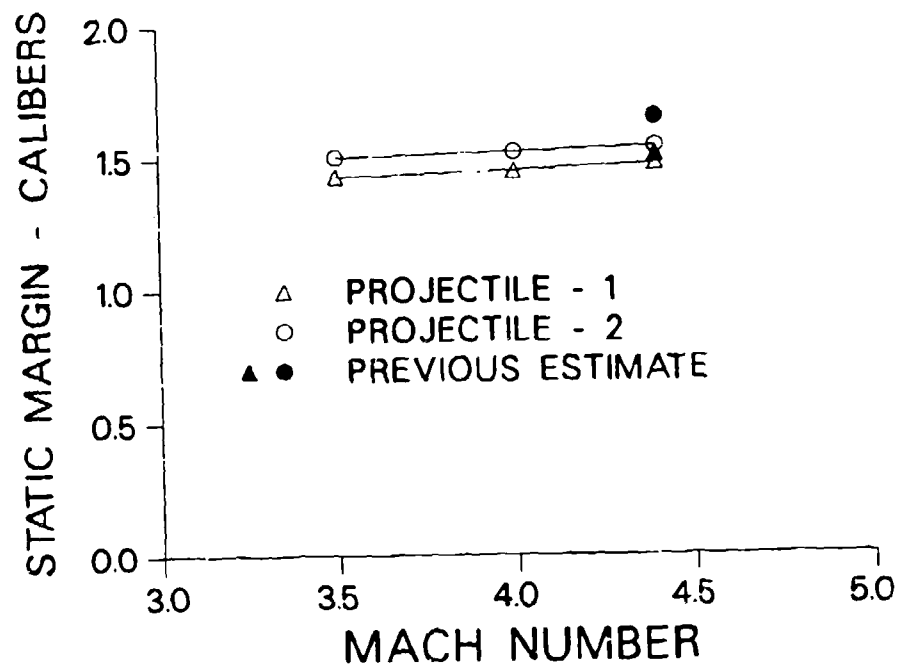


Figure 6. Variation of static margin with Mach number.

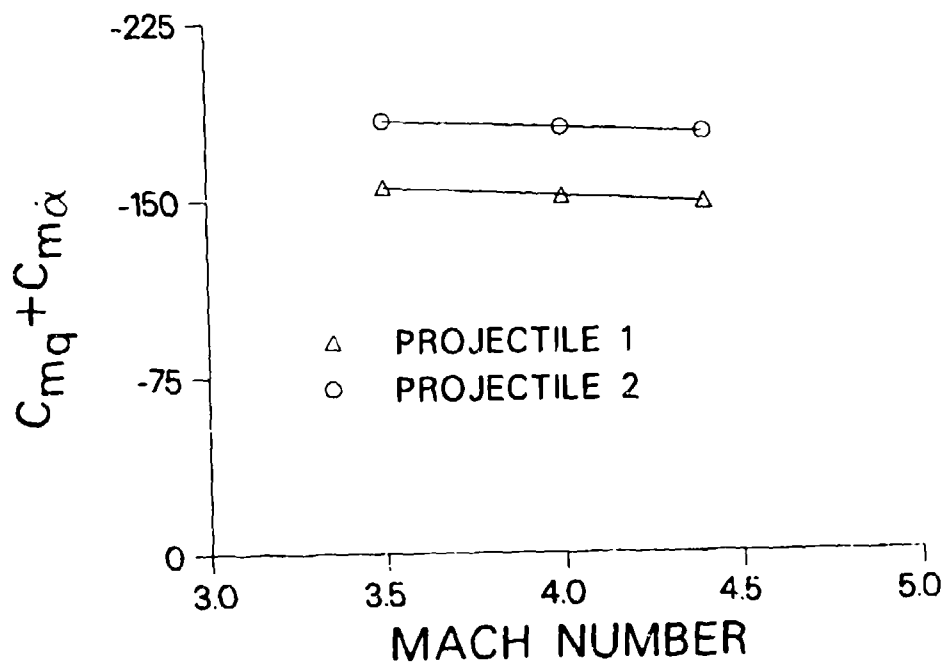


Figure 7. Variation of pitch-damping moment coefficient with Mach number.

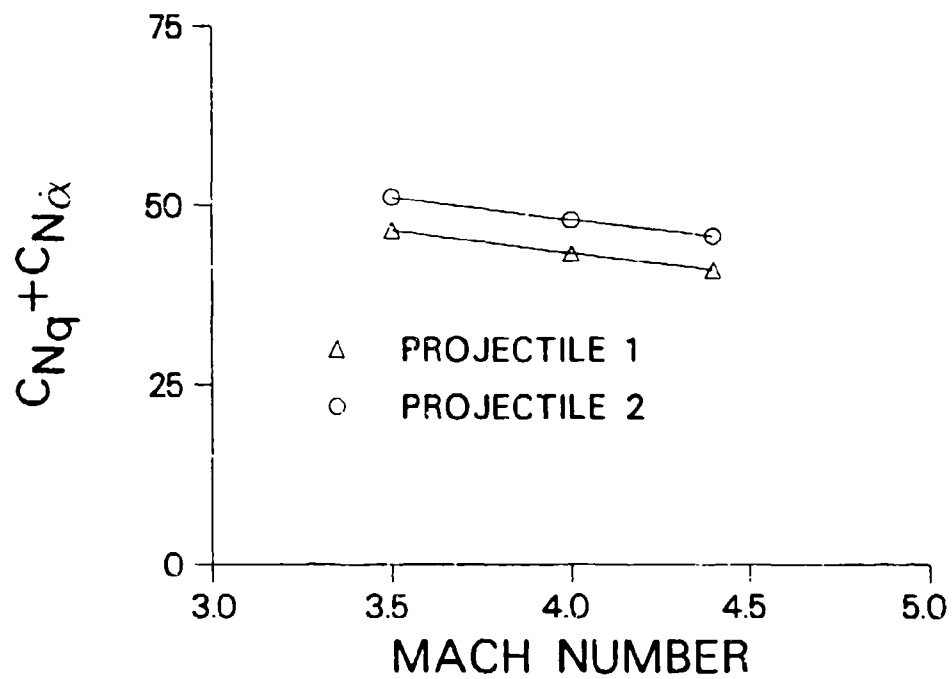


Figure 8. Variation of pitch-damping force coefficient with Mach number.

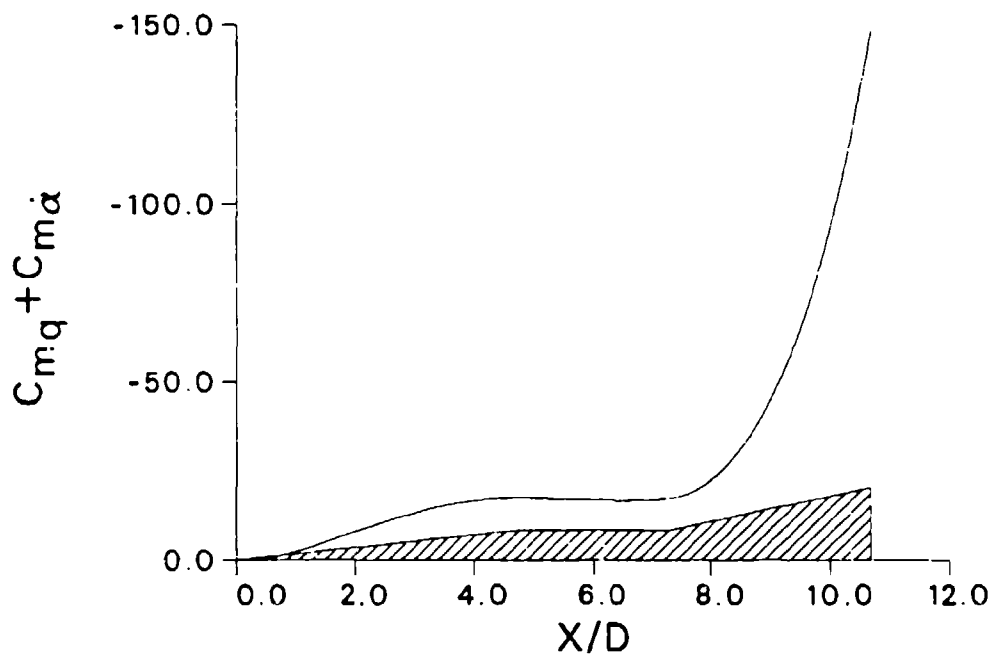


Figure 9. Development of pitch-damping moment coefficient over projectile # 1, Mach 4.4

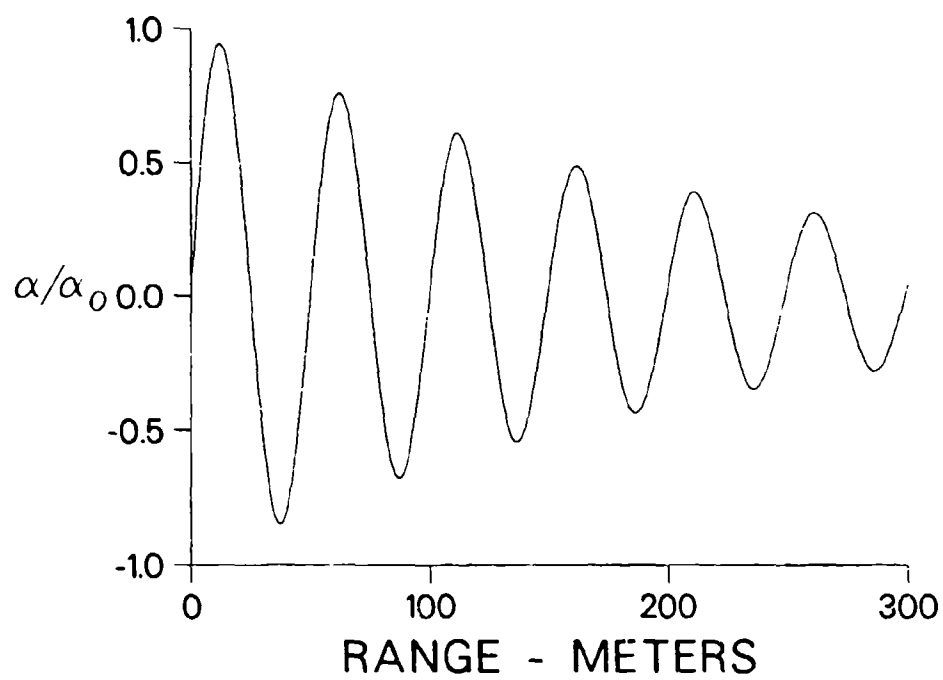


Figure 10. Pitching motion as a function of range - Projectile # 1.

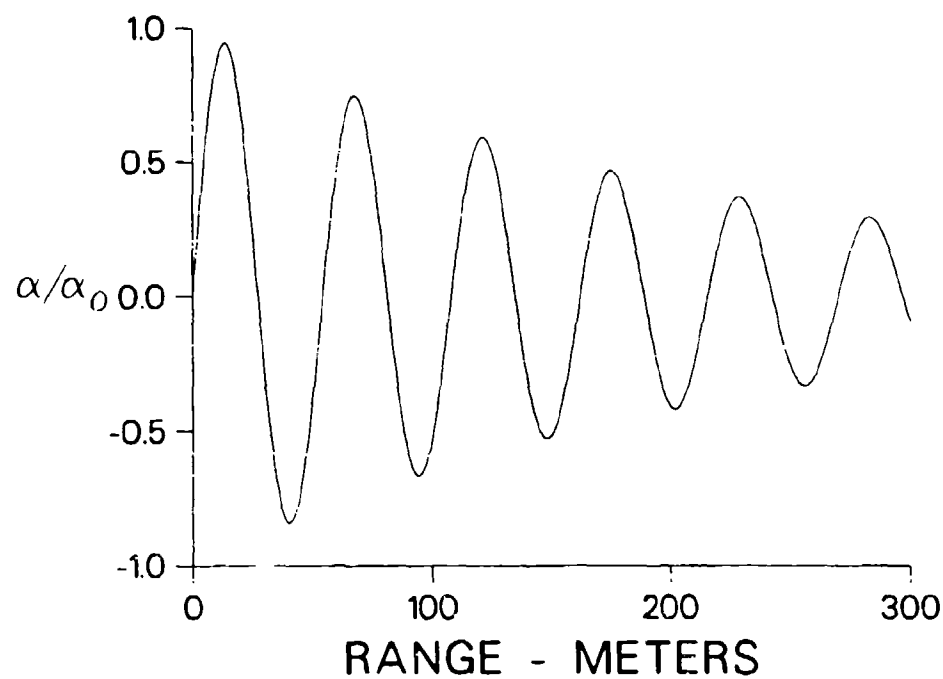


Figure 11. Pitching motion as a function of range - Projectile # 2.

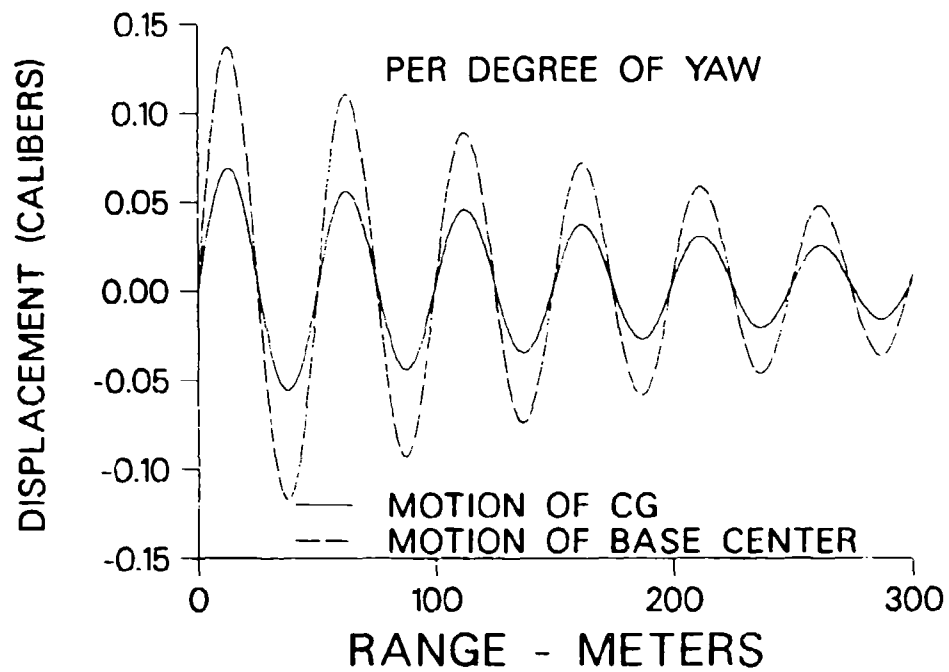


Figure 12. Swerving motion as a function of range - Projectile # 1.

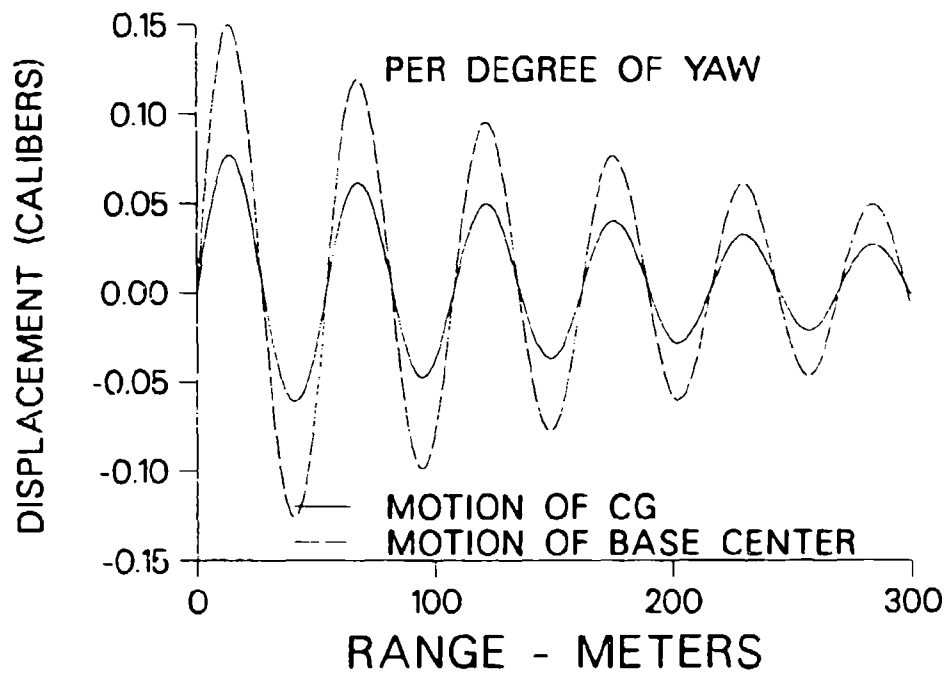
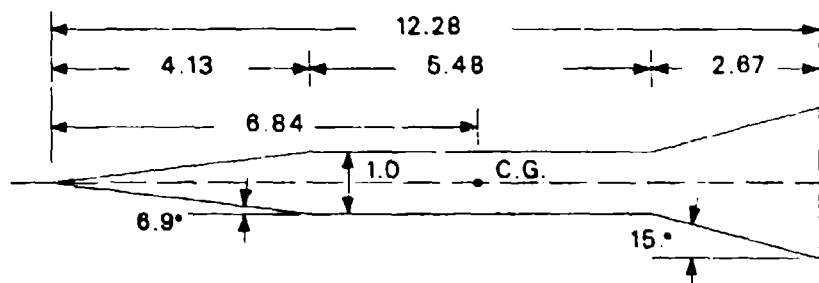
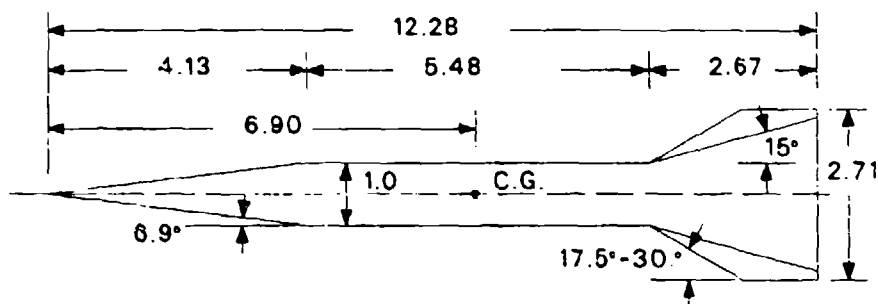


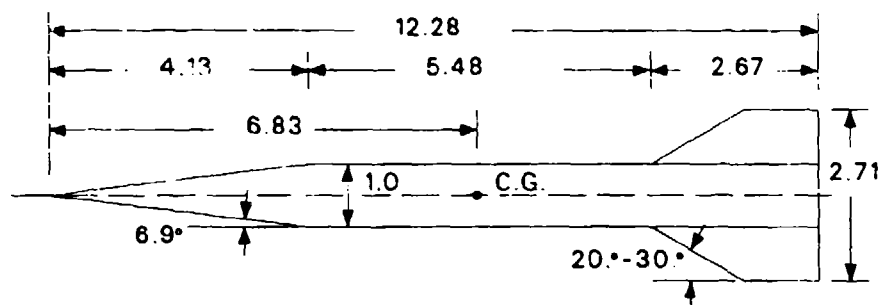
Figure 13. Swerving motion as a function of range - Projectile # 2.



ALL DIMENSIONS IN CALIBERS (ONE CALIBER = 40.6 mm)
Figure 14. Schematic of flared projectile configuration.



ALL DIMENSIONS IN CALIBERS (ONE CALIBER = 40.6 mm.)
Figure 15. Schematic of flared projectile with strakes.



ALL DIMENSIONS IN CALIBERS (ONE CALIBER = 40.6 mm)
Figure 16. Schematic of finned projectile configuration.

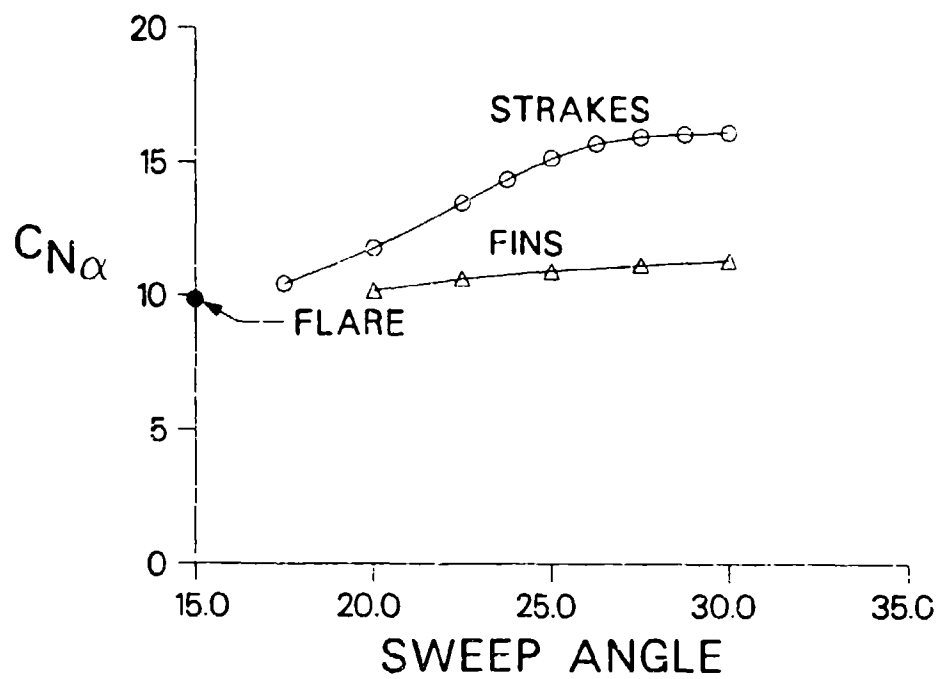


Figure 17. Variation of normal force coefficient slope with sweep angle.

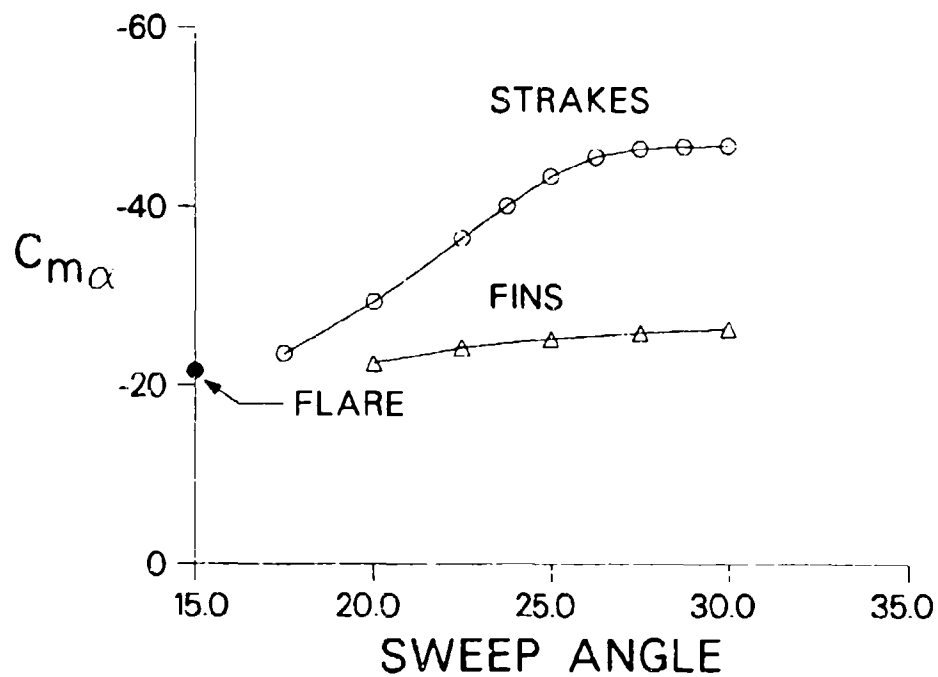


Figure 18. Variation of pitching moment coefficient slope with sweep angle.

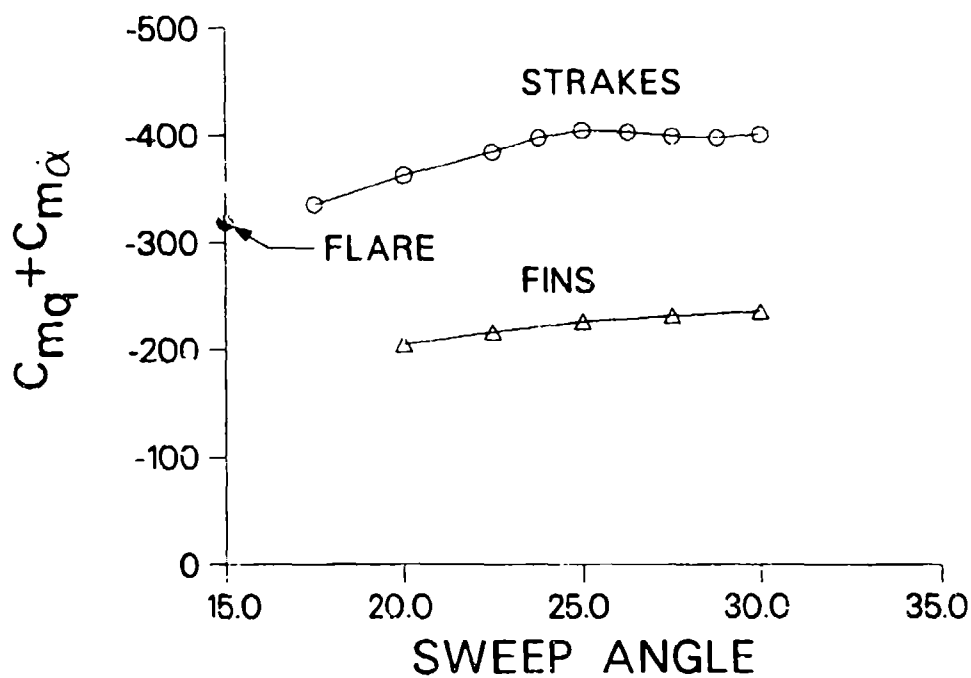


Figure 19. Variation of pitch-damping moment coefficient with sweep angle.

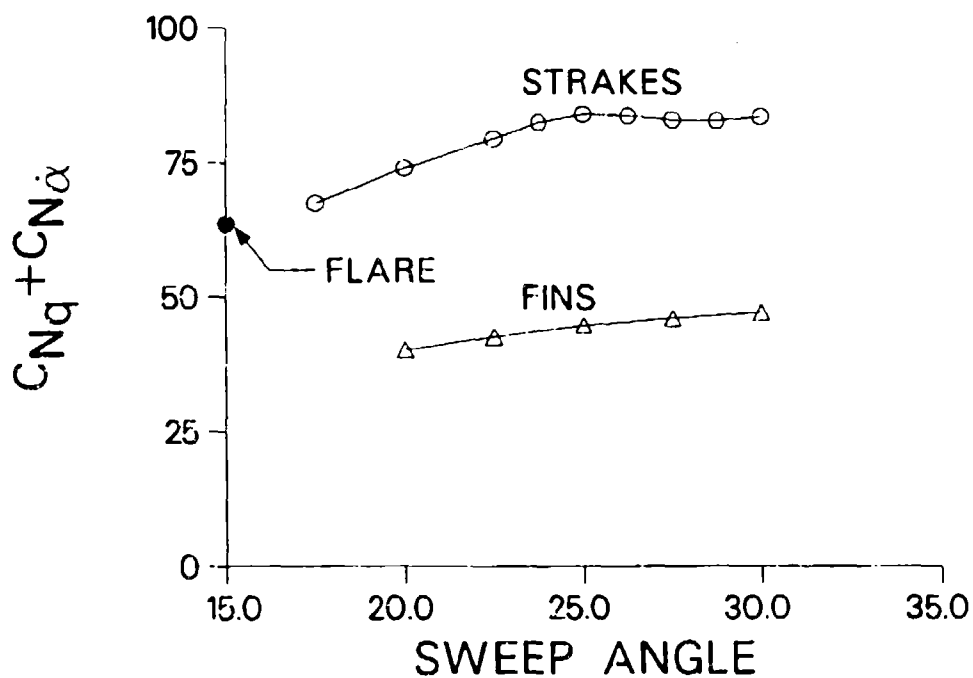


Figure 20. Variation of pitch-damping force coefficient with sweep angle.

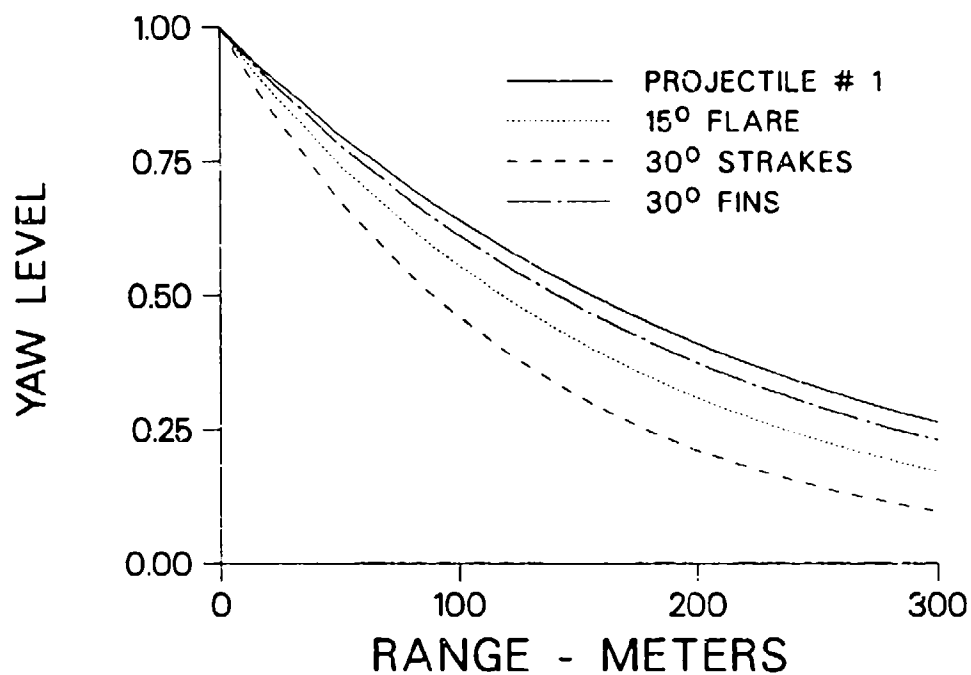


Figure 21. Yawing-damping as a function of range for the improved designs compared with one of the initial designs.

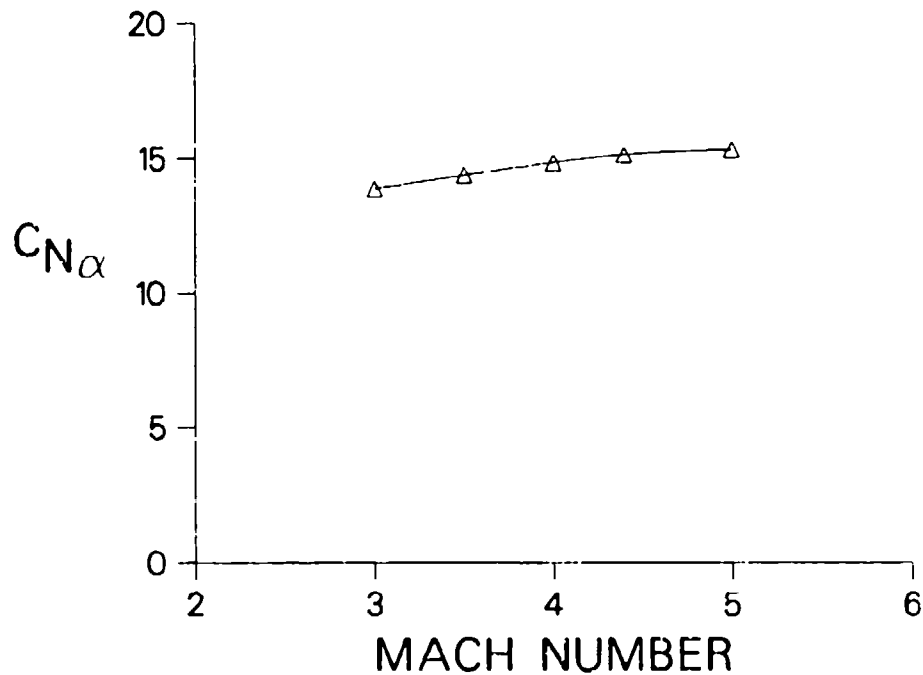


Figure 22. Variation of normal force coefficient slope with Mach number, flared projectile with 25° strakes.

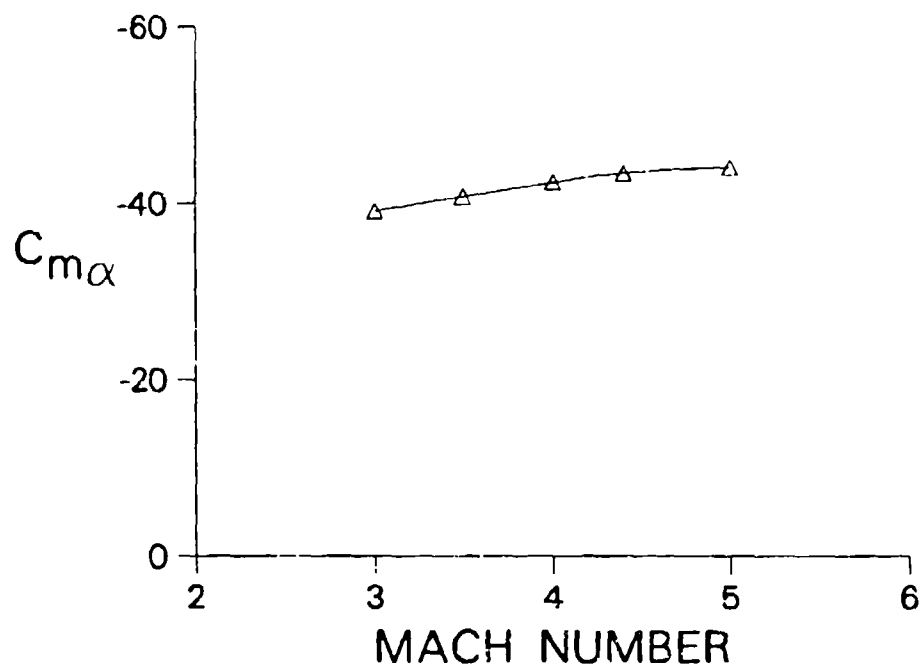


Figure 23. Variation of pitching moment coefficient slope with Mach number, flared projectile with 25° strakes.

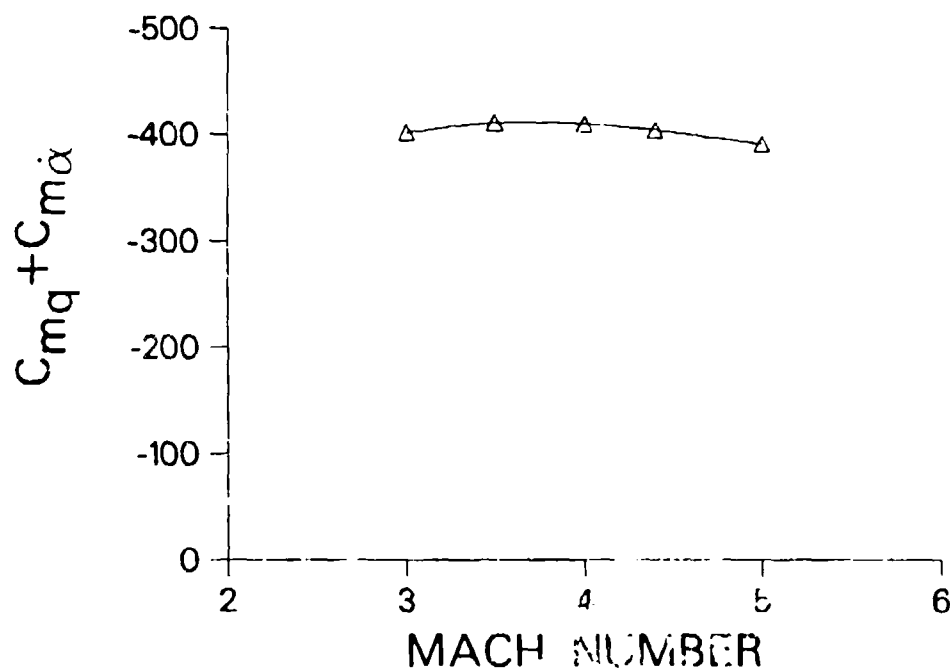


Figure 24. Variation of pitch-damping moment coefficient with Mach number, flared projectile with 25° strakes.

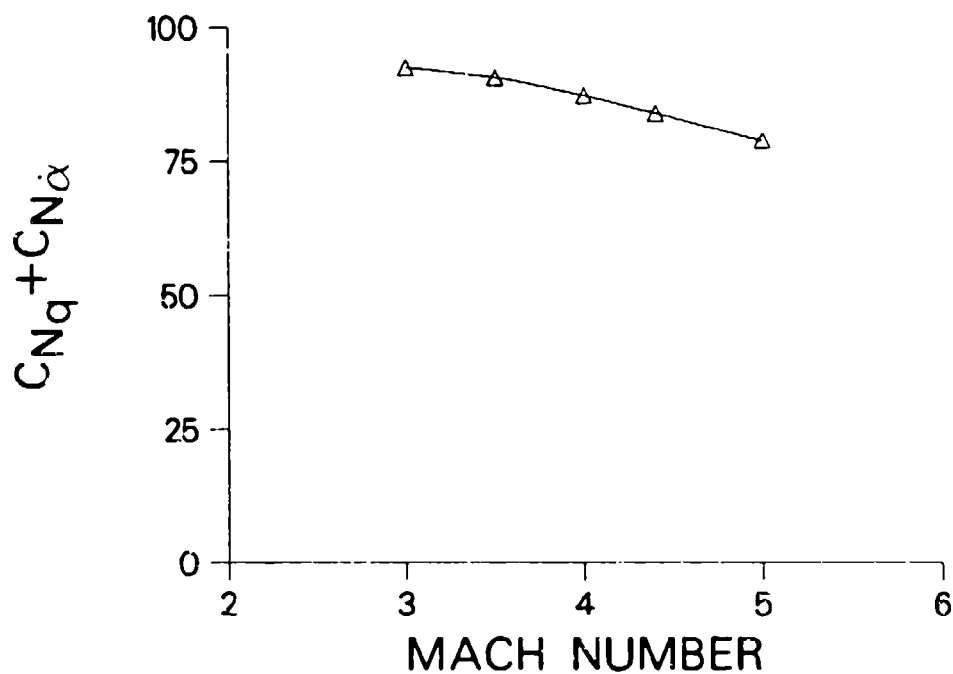


Figure 25. Variation of pitch-damping force coefficient with Mach number, flared projectile with 25° strakes.

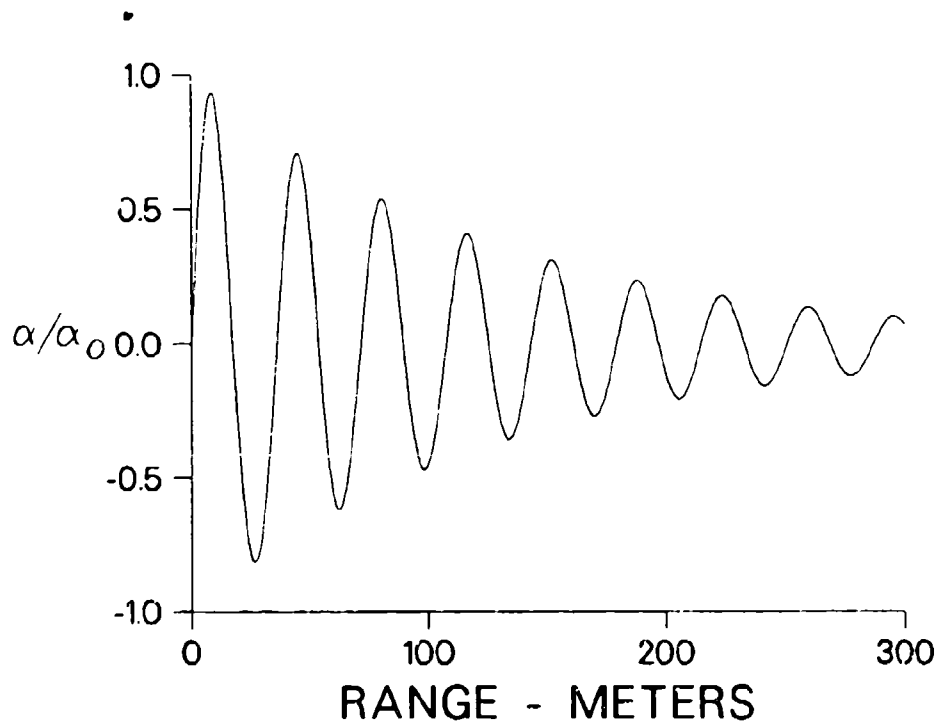


Figure 26. Pitching motion as a function of range, flared projectile with 25° strakes.

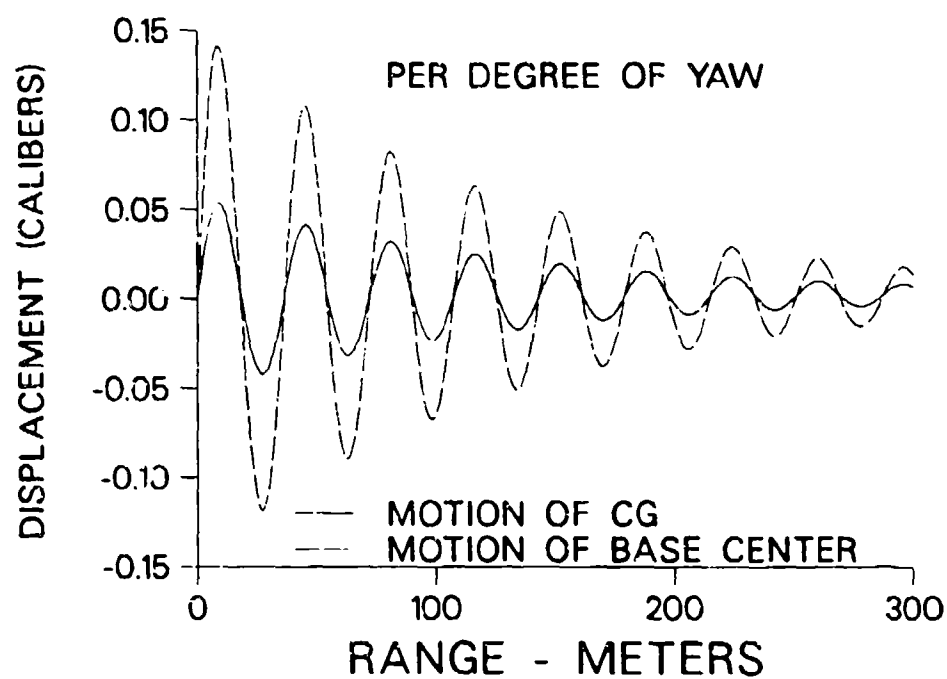


Figure 27. Swerving motion as a function of range, flared projectile with 25° strakes.

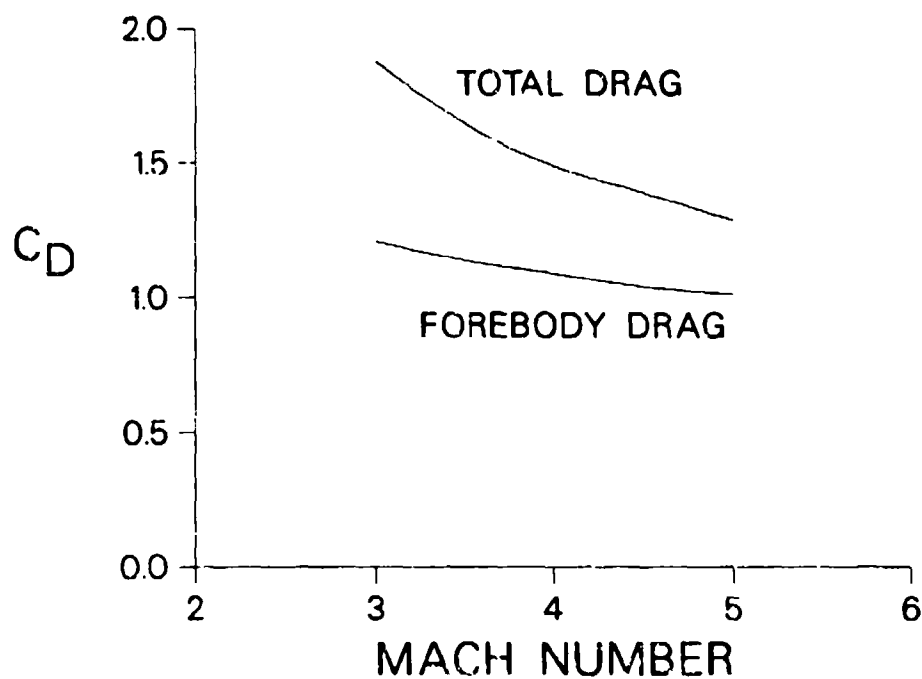


Figure 28. Variation of drag coefficient with Mach number, flared projectile with 25° strakes.

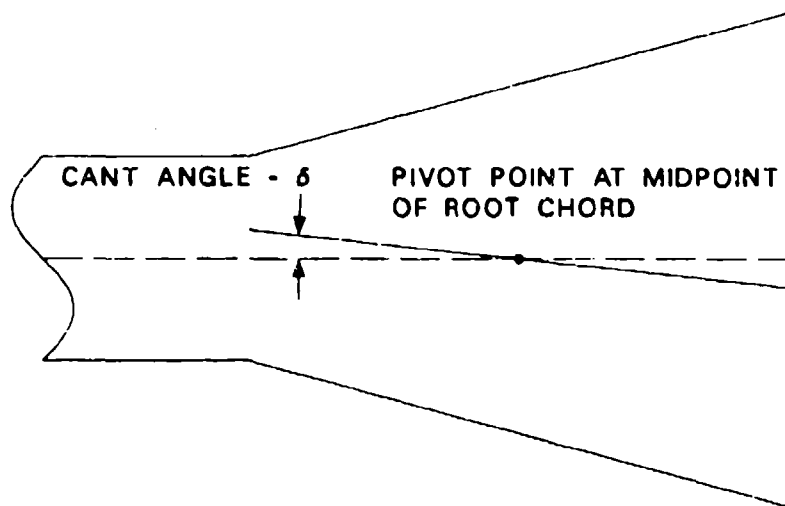


Figure 29. Schematic showing canted strakes.

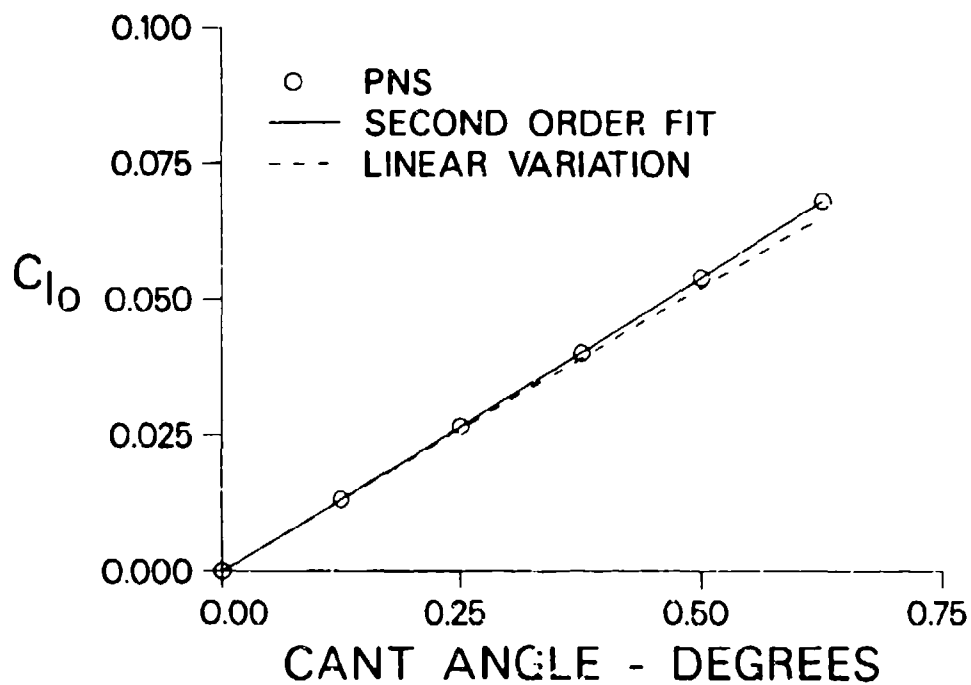


Figure 30. Variation of roll-producing moment coefficient with cant angle.

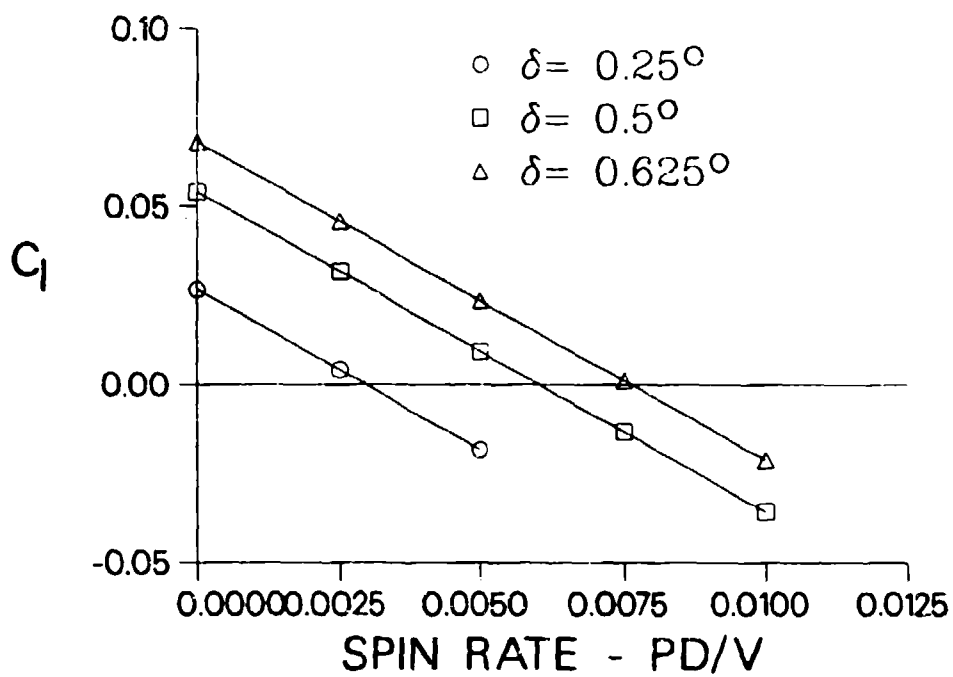


Figure 31. Variation of roll moment with spin rate for various cant angles.

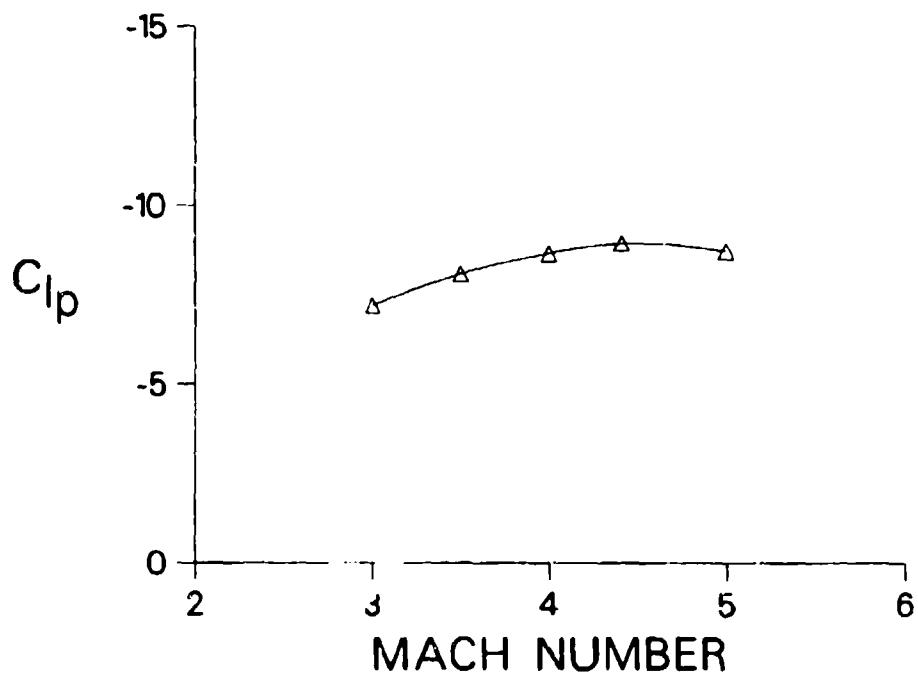


Figure 32. Variation of roll-damping coefficient with Mach number.

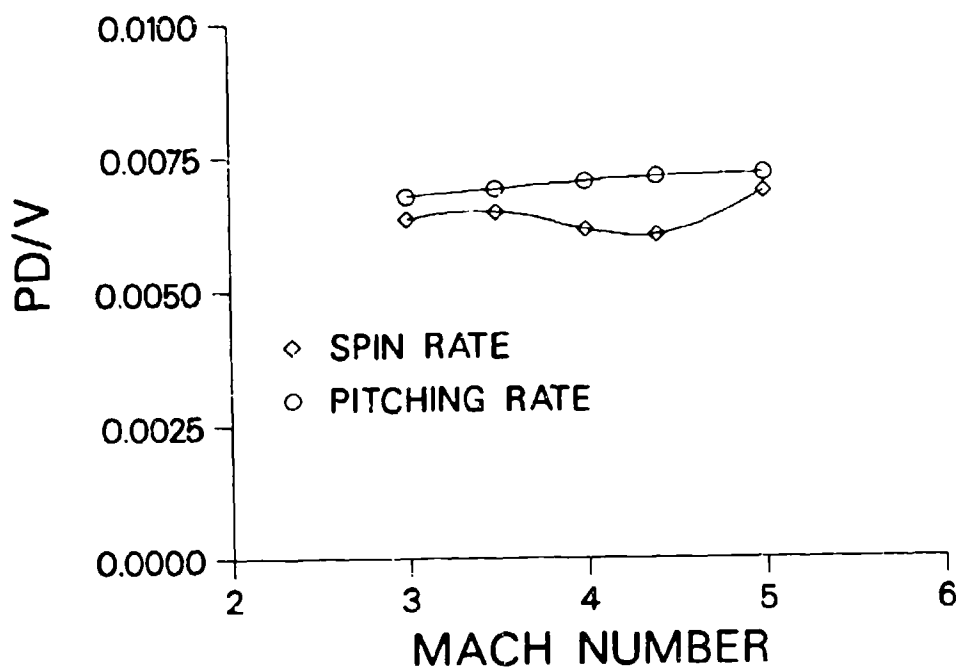


Figure 33. Variation of equilibrium spin rate with Mach number.

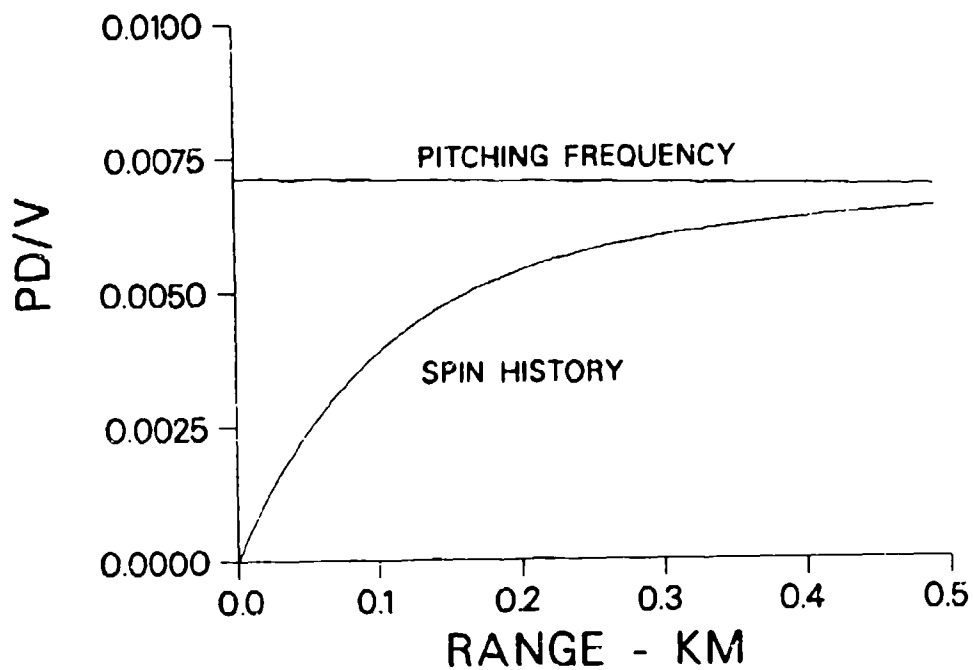


Figure 34. Spin history for 0.5° cant angle.

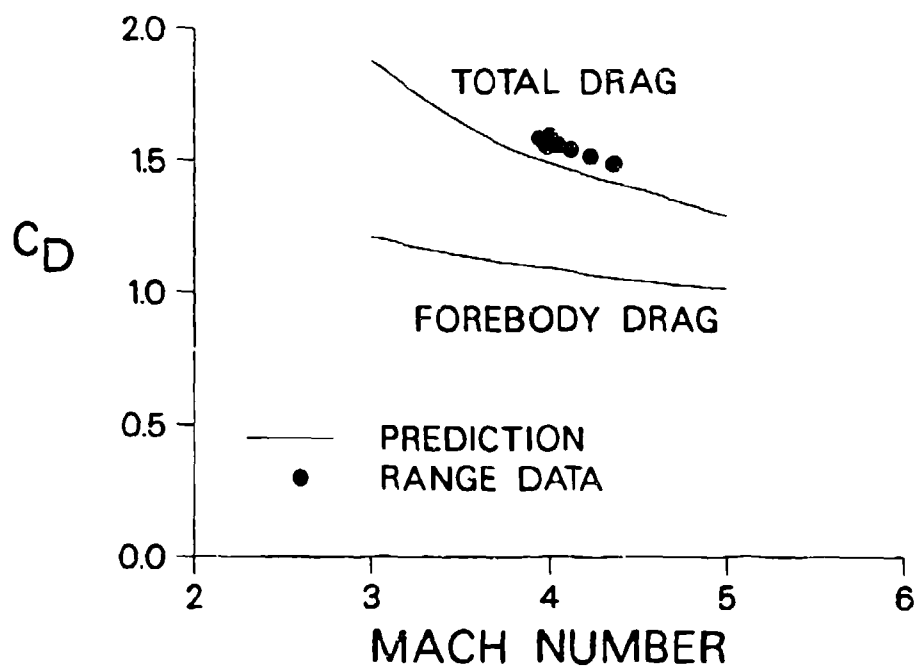


Figure 35. Comparison of measured and predicted drag coefficient, flared projectile with 25° strakes.

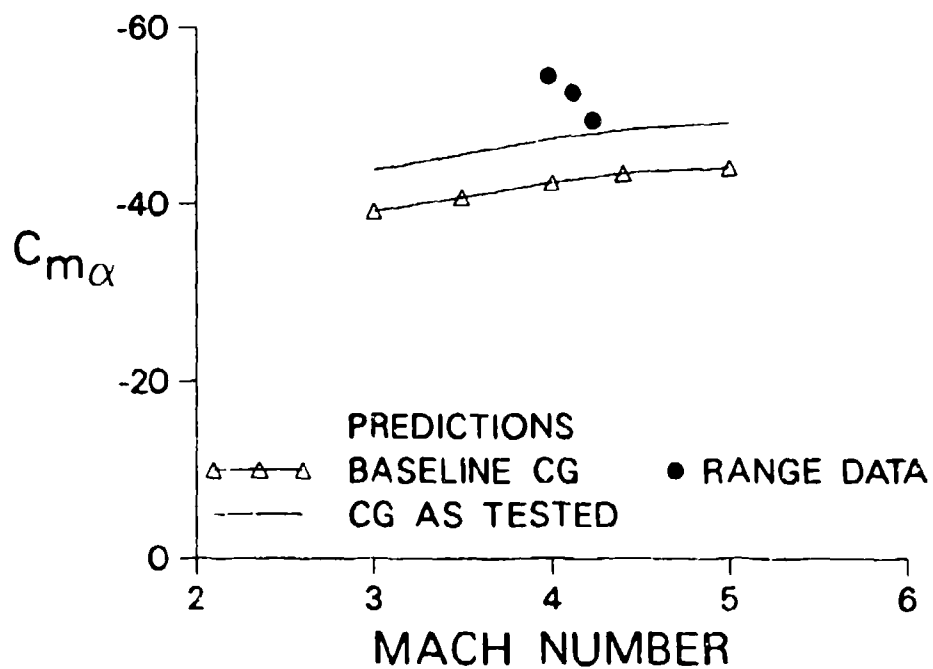


Figure 36. Comparison of measured and predicted pitching moment coefficient, flared projectile with 25° strakes.

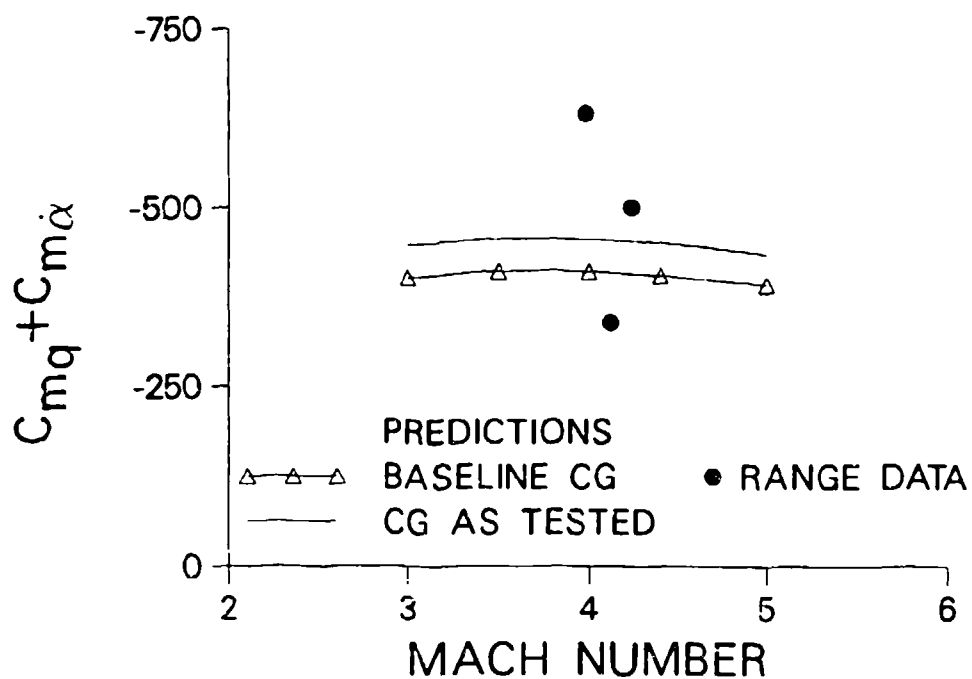


Figure 37. Comparison of measured and predicted pitch-damping moment coefficient, flared projectile with 25° strakes.

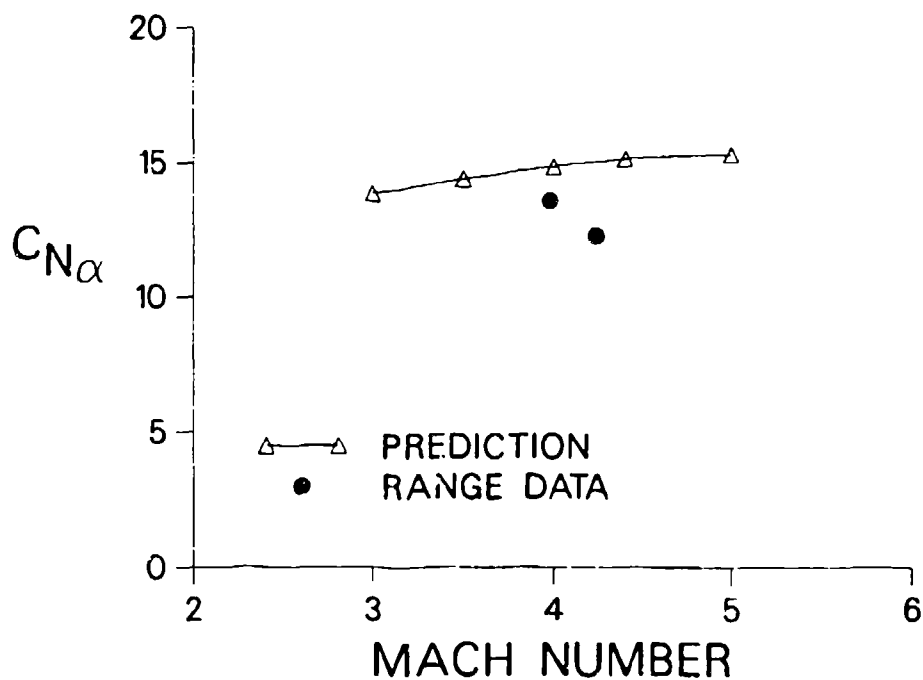


Figure 38. Comparison of measured and predicted normal force coefficient, flared projectile with 25° strakes.

INTENTIONALLY LEFT BLANK.

References

1. Schiff, L.B., and Steger, J.L., "Numerical Simulation of Steady Supersonic Viscous Flow," AIAA Journal, Vol. 18, No. 12, December 1980, pp. 1421-1430.
2. Sturek, W.B., M. D.C., Guidos, B.J., and Nietubicz, C.J., "Navier-Stokes Computational Study of the Influence of Shell Geometry on the Magnus Effect at Supersonic Speeds," U.S. Army Ballistic Research Laboratory, Aberdeen Proving Ground, Maryland, Technical Report BRL-TR-2501, June 1983. (AD A130630)
3. Weinacht, P., Guidos, B.J., Kayser, L.D., and Sturek, W.B., "PNS Computations for Spinning and Fin-Stabilized Projectiles at Supersonic Velocities," U.S. Army Ballistic Research Laboratory, Aberdeen Proving Ground, Maryland, Memorandum Report BRL-MR-3464, September 1985. (AD A160393)
4. Danberg, J.E., Sigal, A., and Celmins, I., "Prediction and Comparison with Measurements of the Aerodynamic Characteristics of Flare-Stabilized XM910 Prototypes," U.S. Army Ballistic Research Laboratory, Aberdeen Proving Ground, Maryland, Technical Report BRL-MR-3752, May 1989.
5. Weinacht, P., and Sturek, W.B., "Computation of the Roll Characteristics of Finned Projectiles," U.S. Army Ballistic Research Laboratory, Aberdeen Proving Ground, Maryland, Technical Report BRL-TR-2931, June 1988. (AD 197875)
6. Weinacht, P., and Sturek, W.B., "Computation of the Roll Characteristics of the M829 Kinetic Energy Projectile and Comparison with Range Data," U.S. Army Ballistic Research Laboratory, Aberdeen Proving Ground, Maryland, Technical Report BRL-TR-3172, November 1990.
7. Weinacht, P., and Sturek, W.B., "Navier-Stokes Computations for Kinetic Energy Projectiles in Steady Coning Motion - A Predictive Capability for Pitch Damping," U.S. Army Ballistic Research Laboratory, Aberdeen Proving Ground, Maryland, Technical Report in preparation.
8. Baldwin, B.S., and Lomax, H., "Thin Layer Approximation and Algebraic Model for Separated Turbulent Flows," AIAA Paper 78-257, 16th Aerospace Sciences Meeting, January, 1978.
9. Beam, R., and Warming, R.F., "An Implicit Factored Scheme for the Compressible Navier-Stokes Equations," AIAA Journal, Vol. 16, No. 4, 1978, pp. 85-129.
10. Rai, M.M., and Chaussee, D.S., "New Implicit Boundary Procedure: Theory and Applications," AIAA Paper 83-0123, Reno, Nevada, January 1983.
11. Lowman, B., Private communication, Science and Technology Associates, Inc., Arlington, Virginia 22203, February 1990.
12. Murphy, C.H., "Free Flight Motion of Symmetric Missiles," U.S. Army Ballistic Research Laboratory, Aberdeen Proving Ground, Maryland, Report No. 1216, July 1963. (AD A442757)

13. Brandon, F.J., Private communication, U.S. Army Ballistic Research Laboratory, Aberdeen Proving Ground, Maryland, February 1990.
14. Devan, L. and Mason, L.A., "Aerodynamics of Tactical Weapons to Mach Number 8 and Angle of Attack 180°: Part II - Computer Program and Users Guide," Naval Surface Weapons Center, Dahlgren, Virginia, Report NSWC-TR 81-358, September 1981.

LIST OF SYMBOLS

a_∞	freestream speed of sound
C_D	drag coefficient
C_{l_p}	net roll moment coefficient
C_{l_0}	roll-producing moment coefficient
C_{l_δ}	variation of roll-producing moment coefficient with cant angle, δ
$C_{l_{\delta^2}}$	variation of roll-producing moment coefficient with square of cant angle
C_{l_p}	roll-damping coefficient
C_{L_α}	slope of the lift coefficient with angle of attack
C_{m_α}	slope of the pitching moment coefficient with angle of attack
$C_{m_q} + C_{m_\alpha}$	pitch-damping moment coefficient
C_{N_α}	slope of the normal force coefficient with angle of attack
$C_{N_q} + C_{N_\alpha}$	pitch-damping force coefficient
D	projectile diameter
e	total energy per unit volume, nondimensionalized by $\rho_\infty a_\infty^2$
$\hat{E}, \hat{F}, \hat{G}$	flux vectors in transformed coordinates
\hat{H}	source term resulting from rotating coordinate frame
I	projectile transverse moment of inertia
J	Jacobian
m	projectile mass
M_∞	freestream Mach number
p	spin rate, as used in roll equations and roll coefficients
pD/V	nondimensional spin rate, nondimensionalized by body diameter, D , and free stream velocity, V
p	pressure, as used in thin-layer Navier-Stokes equations, nondimensionalized by $\rho_\infty a_\infty^2$
p_∞	freestream static pressure nondimensionalized by $\rho_\infty a_\infty^2$
Re	Reynolds number, $a_\infty \rho_\infty D / \mu_\infty$
\hat{S}	viscous flux vector in transformed coordinates
S_{ref}	reference cross-sectional area of projectile, $\pi D^2/4$
u, v, w	velocity components in x, y, and z directions, nondimensionalized by a_∞
U, V, W	Contravariant velocities of the transformed Navier-Stokes equations
x, y, z	Cartesian coordinates with respect to the body, nondimensionalized by D

Note: Moment coefficients are scaled as follows; $M / \frac{1}{2} \rho_\infty a_\infty^2 M_\infty^2 D S_{ref}$

Force coefficients are scaled as follows; $F / \frac{1}{2} \rho_\infty a_\infty^2 M_\infty^2 S_{ref}$

Greek Symbols

α	angle of attack
γ	ratio of specific heats, as used in Navier-Stokes equations

δ	cant angle of strakes
λ	damping rate of projectile
μ	laminar viscosity
μ_t	turbulent viscosity
ξ, η, ζ	transformed coordinates in Navier-Stokes equations
ρ	density
ρ_∞	freestream density
Ω_c	coning rate of projectile, nondimensionalized by D/a_∞

<u>No. of Copies</u>	<u>Organization</u>	<u>No. of Copies</u>	<u>Organization</u>
2	Administrator Defense Technical Info Center ATTN: DTIC-DDA Cameron Station Alexandria, VA 22304-6145	1	Commander U.S. Army Missile Command ATTN: AMSMI-RD-CS-R (DOC) Redstone Arsenal, AL 35898-5010
1	Commander U.S. Army Materiel Command ATTN: AMCAM 5001 Eisenhower Ave. Alexandria, VA 22333-0001	1	Commander U.S. Army Tank-Automotive Command ATTN: AMSTA-JSK (Armor Eng. Br.) Warren, MI 48397-5000
1	Director U.S. Army Research Laboratory ATTN: AMSRL-OP-CI-AD, Tech Publishing 2800 Powder Mill Rd. Adelphi, MD 20783-1145	1	Director U.S. Army TRADOC Analysis Command ATTN: ATRC-WSR White Sands Missile Range, NM 88002-5502
1	Director U.S. Army Research Laboratory ATTN: AMSRL-OP-CI-AD, Records Management 2800 Powder Mill Rd. Adelphi, MD 20783-1145	(Class. only) 1	Commandant U.S. Army Infantry School ATTN: ATSH-CD (Security Mgr.) Fort Benning, GA 31905-5660
2	Commander U.S. Army Armament Research, Development, and Engineering Center ATTN: SMCAR-TDC Picatinny Arsenal, NJ 07806-5000	(Unclass. only) 1	Commandant U.S. Army Infantry School ATTN: ATSH-WCB-O Fort Benning, GA 31905-5000
1	Director Benet Weapons Laboratory U.S. Army Armament Research, Development, and Engineering Center ATTN: SMCAR-CCB-TL Watervliet, NY 12189-4050	1	WL/MNOI Eglin AFB, FL 32542-5000 <u>Aberdeen Proving Ground</u>
1	Director U.S. Army Advanced Systems Research and Analysis Office (ATCOM) ATTN: AMSAT-R-NR, M/S 219-1 Ames Research Center Moffett Field, CA 94035-1000	2	Dir, USAMSAA ATTN: AMXSY-D AMXSY-MP, H. Cohen
		1	Cdr, USATECOM ATTN: AMSTE-TC
		1	Dir, USAERDEC ATTN: SCBRD-RT
		1	Cdr, USACBDCOM ATTN: AMSCB-CII
		1	Dir, USARL ATTN: AMSRL-SL-I
		5	Dir, USARL ATTN: AMSRL-OP-AP-L

<u>No. of Copies</u>	<u>Organization</u>
3	Commander U.S. Army Armament Research, Development, and Engineering Center ATTN: SMCAR-AET, C. Ng H. Hudgins J. Grau Picatinny Arsenal, NJ 07806-5000
1	Commander U.S. Army Armament Research, Development, and Engineering Center ATTN: SMCAR-FSP-A(1), Ken Kendl Picatinny Arsenal, NJ 07806-5000
1	DARPA ATTN: Dr. Peter Kemmey 3761 North Fairfax Dr. Arlington, VA 22203-1714
2	Science and Technology Associates, Inc. ATTN: Dr. Alan Glasser Mr. Bruce Lohman 1700 North Moore St. Arlington, VA 22209
1	Los Alamos National Laboratory ATTN: Mr. Bill Hogan, MS G770 Los Alamos, NM 87545
2	Interferometrics, Inc. ATTN: Dr. Eric L. Strobe! Mr. Rene Lariva Vienna, VA 22180

<u>No. of Copies</u>	<u>Organization</u>
	<u>Aberdeen Proving Ground</u>
13	Dir, USARL ATTN: AMSRL-WT-W, Dr. C. Murphy AMSRL-WT-WB, Dr. W. D'Amico AMSRL-CI-C, Dr. W. Sturek AMSRL-WT-IB, Dr. E. Schmidt Dr. P. Plostins Mr. V. Oskay Mr. C. Nietubicz Dr. J. Sahu Mr. P. Weinacht Mr. H. Edge Mr. B. Guidos Mr. E. Ferry AMSRL-WT-TC, Dr. W. de Rosset

USER EVALUATION SHEET/CHANGE OF ADDRESS

This Laboratory undertakes a continuing effort to improve the quality of the reports it publishes. Your comments/answers to the items/questions below will aid us in our efforts.

1. ARL Report Number ARL-TR-468 Date of Report June 1994

2. Date Report Received _____

3. Does this report satisfy a need? (Comment on purpose, related project, or other area of interest for which the report will be used.) _____

4. Specifically, how is the report being used? (Information source, design data, procedure, source of ideas, etc.) _____

5. Has the information in this report led to any quantitative savings as far as man-hours or dollars saved, operating costs avoided, or efficiencies achieved, etc? If so, please elaborate. _____

6. General Comments. What do you think should be changed to improve future reports? (Indicate changes to organization, technical content, format, etc.) _____

CURRENT
ADDRESS

Organization

Name

Street or P.O. Box No.

City, State, Zip Code

7. If indicating a Change of Address or Address Correction, please provide the Current or Correct address above and the Old or Incorrect address below.

OLD
ADDRESS

Organization

Name

Street or P.O. Box No.

City, State, Zip Code

(Remove this sheet, fold as indicated, tape closed, and mail.)
(DO NOT STAPLE)